Universidad Autónoma de San Luis Potosí
Facultad de Ingeniería
Centro de Investigación y Estudios de Posgrado

Modelado, Análisis y Control de Microrredes de CA en Estado Estacionario

T E S I S

Que para obtener el grado de:

Doctor en Ingeniería Eléctrica
con Opción en Control Automático

Presenta:

M.I. Gibran David Agundis Tinajero

Asesor:

Dr. Juan Segundo Ramírez

Co-asesor:

Dra. Nancy Visairo Cruz

San Luis Potosí, S. L. P. Diciembre de 2018

UASLP
Universidad Autónoma de San Luis Potosí

FACULTAD DE INGENIERÍA

18 de octubre de 2018

M.I. GIBRAN DAVID AGUNDIS TINAJERO
P R E S E N T E.

En atención a su solicitud de Temario, presentada por los **Dres. Juan Segundo Ramírez y Nancy Visairo Cruz,** Asesor y Co-asesor de la Tesis que desarrollará Usted con el objeto de obtener el Grado de **Doctor en Ingeniería Eléctrica**, me es grato comunicarle que en la Sesión del H. Consejo Técnico Consultivo celebrada el día 18 de octubre del presente año, fue aprobado el Temario propuesto:

TEMARIO:

"Modelado, Análisis y Control de Microrredes de CA en Estado Estacionario"

Introducción.

1. Fundamentos de microrredes de CA.
2. Cálculo del estado estacionario periódico de microrredes de CA en los dominios del tiempo y la frecuencia.
3. Control jerárquico para microrredes de CA en modo isla.
4. Inicialización basada en flujos de potencia de métodos en el dominio del tiempo para el cálculo rápido del estado estacionario de microrredes de CA no sinusoidales.

Conclusión.
Bibliografía.

"MODOS ET CUNCTARUM RERUM MENSURAS AUDEBO"

A T E N T A M E N T E

M. I. JORGE ALBERTO PÉREZ GONZÁLEZ
DIRECTOR.

UNIVERSIDAD AUTÓNOMA DE SAN LUIS POTOSÍ
FACULTAD DE INGENIERÍA
DIRECCIÓN

Copia. Archivo.
*etn.

95 AÑOS DE AUTONOMÍA
Primera Universidad Autónoma de México

www.uaslp.mx

Av. Manuel Nava 8
Zona Universitaria • CP 78290
San Luis Potosí, S.L.P.
tel (444) 826 2330 al39
fax (444) 826 2336

UNIVERSIDAD AUTÓNOMA DE SAN LUIS POTOSÍ

FACULTAD DE INGENIERÍA

Área de Investigación y Estudios de Posgrado

Aclaración

El presente trabajo que lleva por título:

Modelado Análisis y Control de Microrredes de CA en Estado Estacionario

se realizó en el periodo febrero de 2015 a diciembre de 2018 bajo la dirección del Dr. Juan Segundo Ramirez y la Dra. Nancy Visairo Cruz.

Originalidad

Por este medio aseguro que he realizado este documento de tesis para fines académicos sin ayuda indebida de terceros y sin utilizar otros medios más que los indicados.

Las referencias e información tomadas directa o indirectamente de otras fuentes se han definido en el texto como tales y se ha dado el debido crédito a las mismas.

El autor exime a la UASLP de las opiniones vertidas en este documento y asume la responsabilidad total del mismo.

Este documento no ha sido sometido como tesis a ninguna otra institución nacional o internacional en forma parcial o total.

Se autoriza a la UASLP para que divulgue este documento de Tesis para fines académicos.

Atentamente

_____

M.I. Gibran David Agundis Tinajero

Índice

UNIVERSIDAD AUTÓNOMA DE SAN LUIS POTOSÍ

Modeling, Analysis and Control of AC Microgrids in Steady-State

by

M.I. Gibran David Agundis Tinajero

A thesis submitted in fulfillment for the
degree of Doctor of Philosophy

in the
Facultad de Ingeniería
Centro de Investigación y Estudios de Posgrado

December 2018

UNIVERSIDAD AUTÓNOMA DE SAN LUIS POTOSÍ

Abstract

Facultad de Ingeniería
Centro de Investigación y Estudios de Posgrado

Doctor of Philosophy

by M.I. Gibran David Agundis Tinajero

The microgrid concept is associated with a group of loads and distributed energy resources, including renewable energy resources and energy storage systems, operating as a controllable subsystem that can work connected to the main power system or independently. As they offer special operative features, important research efforts are currently underway to develop mathematical models and techniques to evaluate and improve their performance, both in the transient and steady state. In this regard, this thesis addresses the modeling, analysis and control of AC microgrids with emphasis on the fast computation of the steady-state solution taking into account hierarchical control schemes and the explicit commutation of the power electronics converters.

Thesis Details and Publications

Thesis Title	Modeling, Analysis and Control of AC Microgrids in Steady-State.
Ph.D. Student	M.I. Gibran David Agundis Tinajero.
Supervisor	Dr. Juan Segundo Ramírez.
Co-supervisor	Dr. Nancy Visairo Cruz.

Journal Publications:

- Gibran Agundis-Tinajero, Juan Segundo-Ramírez, Nancy Visairo-Cruz, Mehdi Savaghebi, Josep M. Guerrero, and Emilio Barocio. Power flow modeling of islanded ac microgrids with hierarchical control. International Journal of Electrical Power & Energy Systems, 105:28, 36, 2019. ISSN 0142-0615. doi: https://doi.org/10.1016/ j.ijepes.2018.08.002.
- G. D. Agundis Tinajero, N. L. Diaz Aldana, A. C. Luna, J. Segundo-Ramirez, N. Visairo, J. M. Guerrero, and J. Vasquez. Extended opf-based hierarchical control for islanded ac microgrids. IEEE Transactions on Power Electronics, pages 1,1, 2018. ISSN 0885-8993. doi: 10.1109/TPEL.2018.2813980.
- G. Agundis-Tinajero, J. Segundo-Ramírez, R. Peña-Gallardo, N. Visairo-Cruz, C. Nuñez-Gutierrez, J. M. Guerrero, and M. Savaghebi. Harmonic issues assessment on pwm vsc-based controlled microgrids using newton methods. IEEE Transactions on Smart Grid, 9(2):1002,1011, March 2018. ISSN 1949-3053. doi: 10.1109/TSG.2016.2574241.

Conference Publications:

- G. Agundis-Tinajero, J. Segundo-Ramírez, N. Visairo-Cruz and R. Peña-Gallardo. Stability and Resonance Analysis of AC Power Electronics-Based Systems. In 2018 IEEE International Autumn Meeting on Power, Electronics and Computing (ROPEC).
- A. E. Saldaña, E. Barocio, A. R. Messina, J. J. Ramos, R. J. Segundo, and G. Agundis-Tinajero. Monitoring harmonic distortion in microgrids using dynamic mode decomposition. In 2017 IEEE Power Energy Society General Meeting, pages 1,5, July 2017. doi: 10.1109/PESGM.2017.8274696.

Works in progress:

- G. Agundis-Tinajero, J. Segundo-Ramírez, et al. Performance Assessment of Shooting Methods Using Parallel Cloud Computing.
- G. Agundis-Tinajero, J. Segundo-Ramírez, et al. Voltage Source Converter Modeling for RTDS Applications.

Dedicated to my parents
M. Concepción Tinajero and J. Candelario Agundis

Acknowledgements

My deepest gratitude to my supervisor, Dr. Juan Segundo Ramírez. Thank you for believing in me, for making me believe in myself, for your time, patience, knowledge and experience both academically and in life. Thank you for encouraging me to always do my best and for helping me improving myself beyond I would have even imagine. Finally, I would like to thank you for these eight years of friendship.

I would also like to thank Dra. Nancy Visairo Cruz, Dr. Rafael Peña Gallardo, Dr. Ciro Nuñez Gutiérrez, Dr. Homero Miranda Vidales, Dr. Emilio Barocio Espejo, Dr. Juan Manuel Ramírez, Dr. Josep M. Guerrero and Dr. Juan C. Vazquez for all their academic and personal support that was fundamental for the development of this work.

Thanks to my colleagues and friends Carlos, Miguel, Aaron, Roberto, Omar, Toro, Sinuhe, Nelson, Adriana, Adolfo, Juan, Alfredo and Eugenio for the time shared with me, their friendship and support.

Thanks to my parents M. Concepcion Tinajero and J. Candelario Agundis, and my siblings Brianda and Iván, for their unconditional support and love.

I would like to express my sincere thanks to the Consejo Nacional de Ciencia y Tecnología (CONACYT) for the financial support during the period of study.

Contents

List of figures

List of tables

"We shall not cease from exploration, and the end of all our exploring will be to arrive where we started, and know the place for the first time."

T. S. Eliot

Introduction

Small isolated grids have existed for a few decades in remote communities where the interconnection with the main electric power system is not possible [1]; however, the concept of microgrids (MGs) was originated due to the integration of distributed energy resources (DER) and controlled loads [2]. The microgrid concept is associated with a group of loads and DER, including renewable energy sources (RES) and energy storage systems (ESS), operating as a controllable subsystem that can work connected to the main power system or independently [1–3]. Since MG offer special operating characteristics, such as, improved reliability, reduced transmission power losses, regulation and local voltage support, improved power management performance, support of transmission and distribution network events, among others [3], they have been introduced as a groundbreaking technology to modernize the electric power systems [3–6].

Due to the complex operation, harmonics, and interactions between the DERs, the MG special operating features demand detailed and efficient mathematical models in order to perform power systems studies, such as, electromagnetic transients, harmonic power flow, harmonic estimation, faults analysis, stability subject to large disturbances within the microgrid or in the utility side, small signal stability, dispatch of distributed generation systems, power quality, etc. Some of these studies are carried out simpler and more efficient in the frequency domain and others in the time domain, additionally, some of these studies are in steady state and others in transient state. However, for any of these scenarios is required the development of appropriate mathematical models of the microgrid components as well as efficient computational algorithms for execution and analysis.

On the other hand, it has been found that in microgrids the variables of control and the grid are coupled, such that, there are effects of the harmonic distortion on the performance of the control systems and the stability of the periodic solution, and vice versa, that must be taken into account. Therefore, there is a close relationship between control systems, harmonics, asymptotic stability, transient and steady-state performance that must be considered in microgrid design and studies in order to not overlook phenomena

or undesirable behaviors when using inappropriate models or techniques [1]. Thus, it is important to evaluate the pertinence and limitation of different mathematical models and techniques employed for analysis and design of microgrids [7, 8].

Regarding the aforementioned, this thesis addresses numerical methods in the time and frequency domain for the fast steady-state computation of AC microgrids, including hierarchical control schemes and the explicit commutation process of the power converters.

Justification

The operating conditions in microgrids often have high harmonic penetration, unbalances, nonlinear elements, dependent frequency parameters, switching phenomena, among others. Therefore, it is necessary to assess if the modeling and analysis approaches of electrical networks based on phasor models and average models are valid in microgrids. Furthermore, it is important to assess if the considerations that allow sequential and decoupled studies remain valid when power electronic based power systems are analyzed.

Thesis objectives

General objective

Develop models and numerical methods to be implemented in a computer considering advanced tools of processing. This will serve to study AC microgrids with a high level of detail and low computation times.

Specific objectives

- Development and implementation of numerical methods for the accelerated computation of the periodic steady-state solutions that allow the use of advanced tools such as cloud computing and parallel processing.
- Development and implementation of the power flow method taking into account hierarchical control schemes.
- Development and implementation of a hierarchical control scheme using the previous numerical methods.
- Development and implementation of a predictor-corrector numerical method for the accelerated computation of the periodic steady-state solutions of controlled nonsinusoidal AC microgrids.

Methodology

In order to arrange sequentially the steps of the development of this research, the methodology will be chronologically ordered in the following activities:

1. Review of state of the art.
2. Formulation and implementation with parallel programming techniques and cloud computing of three Newton methods in the time domain to compute the periodic steady-state solutions.
3. Formulation and solution of the hierarchical controlled power flow.
4. Development and implementation of a hierarchical control scheme for islanded AC microgrids.
5. Formulation and implementation of a predictor-corrector method for the accelerated computation of the periodic steady-state solutions of controlled nonsinusoidal AC microgrids.

Thesis outline

The thesis is organized as follows:

Chapter 1: Fundamentals of AC microgrids

In this chapter, the basic AC microgrid control schemes are presented in detail including the block diagrams of each control. Additionally, case studies showing the controls behavior are addressed. On the other hand, stability and resonance issues that can be found in microgrids are discussed and analyzed.

Chapter 2: Periodic steady-state computation of AC microgrids in time and frequency domains

In this chapter, methods in the time and frequency domain for the computation of the steady-state solution of controlled AC microgrids are presented. The methods are described in detail and case studies for their evaluation are analyzed, furthermore, the advantages and drawbacks of the different approaches are presented.

Chapter 3: Hierarchical control of islanded AC microgrids

In this chapter, the extended power flow method presented in Chapter 2 is used for the development of a hierarchical control scheme for islanded AC microgrids.

Chapter 4: Power-flow-based initialization of fast time-domain methods for the steady-state computation of nonsinusoidal AC microgrids

In this chapter, the time and frequency domain methods described in Chapter 2 are used to develop a predictor-corrector scheme for the fast computation of the steady-state solution of controlled AC microgrids.

Chapter 1

Fundamentals of AC microgrids

For more than one century, centralized electric power generation has been used to feed the industrial and domestic electric demand across the world; however, in the last decades, the research and development of renewable energy technologies have been increasing and getting stronger, such that, the use of distributed generation (DG) units with power electronic interfaces (DC/AC or AC/DC/AC) is becoming more common in electric power systems such as AC and DC microgrids (MGs) [2, 9]. This has brought the need for the development of sophisticated control strategies and analysis techniques, with the purpose of maintaining a proper and reliable operation of the MG [1, 10, 11].

Since the MG concept was developed, a big research effort has been focus to maximize the reliability and potential benefits that the MGs can offer. Some of the issues that can be found on MGs arise from assumptions commonly applied to conventional power systems which are invalid for MGs, such as, perfectly balanced systems, no harmonic distortion, etc. [1, 3], furthermore, it has been found that the variables of MG controls and the grid are coupled and there are interactions between them, such that, the harmonic distortion affects the performance of the control systems and the stability of the periodic solution must be taken into account [1]. In this way, in the past years, new control schemes have been proposed to cope with different issues that can be found in MGs, such as, voltage droops, frequency deviations, power quality, power sharing, among others; nonetheless, most of the control improvements have been based on basic primary and secondary control schemes for both, grid-connected and islanded modes.

Regarding the aforementioned, this chapter presents the basic primary and secondary AC microgrid controls used as base for sophisticated control schemes. Additionally, two case studies are presented to show the necessity for the development of hierarchical control schemes, analysis methods, and detailed component models in order to avoid phenomena or undesirable behaviors of the system.

1.1 AC microgrid controls

1.1.1 Primary controls for AC microgrids

Primary controls are the first level in the control hierarchy, featuring the fastest response. They are used to share power with the main grid or to feed a local load in a controlled manner by means of local measurements; this can be done via controlling the current injected by the DG unit or controlling the voltage of the inverter output. Resulting in current and voltage controlled strategies [1, 3, 11].

The current-controlled strategies are used to inject active and reactive power, lacking the capacity to regulate the system frequency or voltage, so they need to work connected to the grid or together with another DG which regulates the frequency and voltage of the MG. In this way, the regulation of the system frequency and voltage can be achieved using voltage-controlled inverters [1]. In any case, the DG units need to be synchronized with the system, if it is connected to the main grid, such that they can work properly. For each different control scheme, the needed information can be the phase angle, the frequency, and the voltage amplitude.

1.1.1.1 Synchronization of power converters

The synchronization task is often defined as the procedure of matching a source with an existing power system so that they are able to work in parallel. During this process, the phase angle, voltage, and frequency of the DG unit are synchronized with the power system [12]. On the other hand, the information provided by the synchronization unit, in addition to the initial synchronization task, are also very useful for different monitoring/control purposes, such as the reference current generation for the converter, adapting controllers to the grid frequency variations, islanding detection, among others [13, 14].

Phase-locked loop. A phase-locked loop (PLL) is a closed-loop nonlinear feedback control system that synchronizes its output in frequency and phase with its input. Three basic parts can be found in almost all PLLs [13]:

- Phase detector (PD): this unit provides a signal which contains the phase error information, i.e., the difference between the real and estimated phase angle. Depending on the PD, some AC ripples may also exist in its output.

- Loop filter (LF): the LF is mainly responsible to filter the AC components of the PD output. The PLL tracking characteristics are also mainly dictated by the LF.
- Voltage-controlled oscillator (VCO): the VCO generates a sinusoidal signal in its output whose angle is equal to the integral of the LF output.

Within three-phase systems, the synchronous reference frame PLL (SRF-PLL) is a standard, being the basic block of almost all advanced PLLs (see Fig. 1.1) [14].

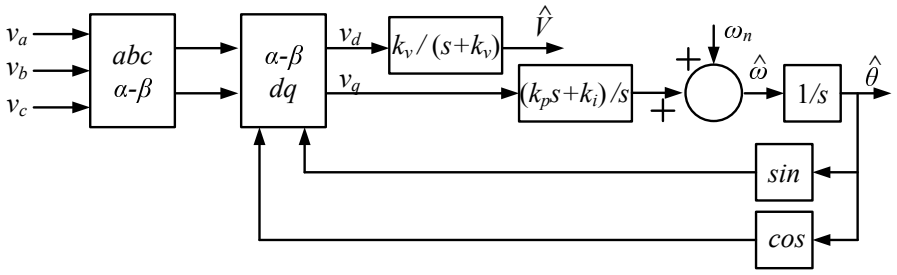

FIGURE 1.1: SRF-PLL block diagram.

1.1.1.2 Grid-forming droop-based control

The grid-forming power converters are controlled working as AC voltage sources having as references the voltage amplitude and frequency [10]. Under islanded operation, the voltage magnitude and frequency of the system have to be regulated, therefore, at least one DG unit assumes this task [10, 15]. In this scheme, the power injection of each DG unit of the islanded system is defined by the frequency/active power (P-ω) and voltage/reactive power (Q-V) droop characteristics [16],

$$\omega = \omega^* - K_n^p P_n \tag{1.1}$$

$$V_n = V_n^* - K_n^q Q_n \tag{1.2}$$

where, ω^* is the nominal angular frequency, V_n^* is the voltage amplitude, and K_n^p and K_n^q are the droop coefficients [16]. As shown in Fig. 1.2, the droop characteristics define the angular frequency of the MG, and the voltage of each DG unit; thus, the percentaje of active and reactive power injected by each DG. Therefore, their selection depends on the quantity of active and reactive power injected due to frequency and voltage deviations, respectively.

The control scheme is composed of an inner current control loop and an outer voltage control loop which define the control signals for operating the conversion stage as an ideal

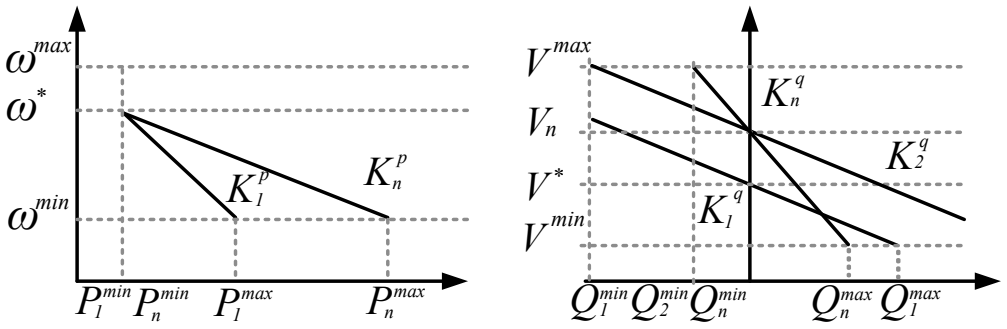

FIGURE 1.2: Conventional droop characteristics.

AC voltage source with a given voltage amplitude and frequency [10]. Fig. 1.3 shows the scheme of the primary controllers working on the *dq* reference frame. The voltage and frequency references for the voltage sources are derived from the droop control loops. To show the behavior of this primary control scheme, an example is presented below.

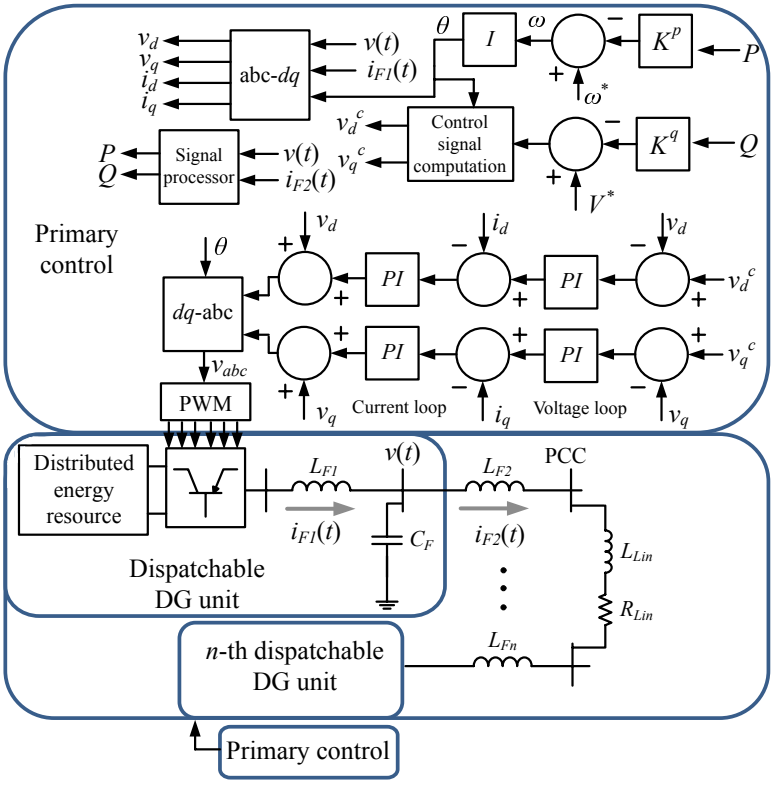

FIGURE 1.3: Basic grid-forming control structure.

The test case (see Fig. 1.4) includes two controlled DG units connected through LCL filters to a point of common coupling (PCC), additionally, a resistive load is connected to the PCC as well.

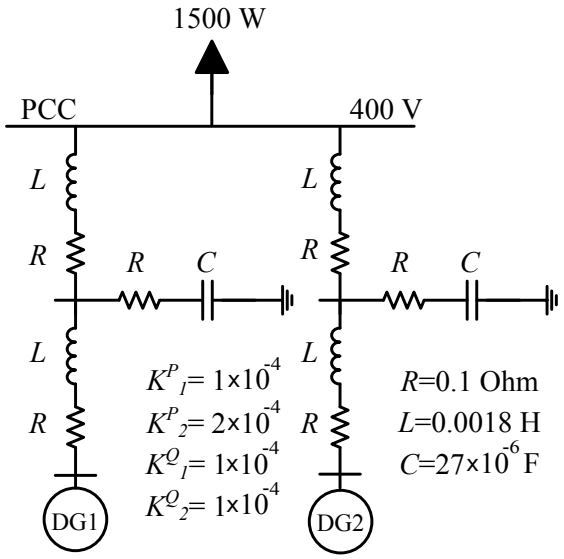

FIGURE 1.4: Single line diagram of the three-phase test system.

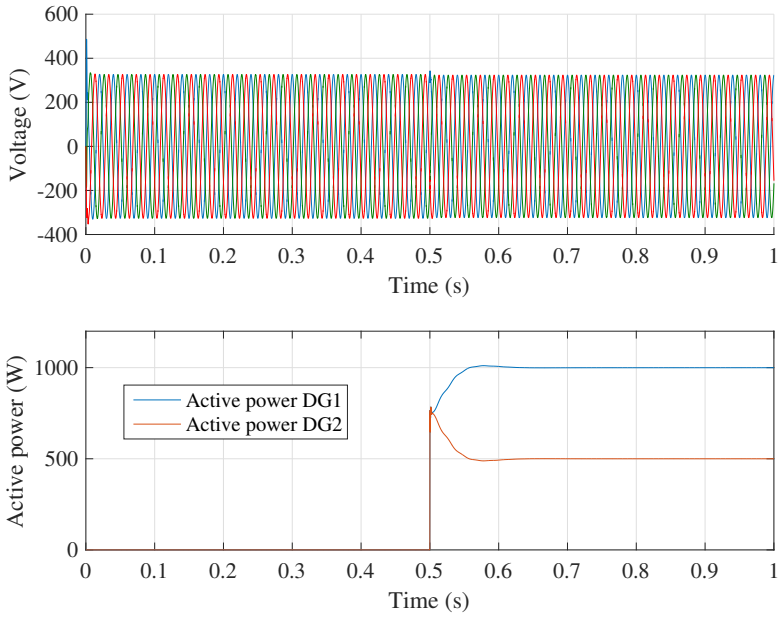

FIGURE 1.5: PCC voltage and DG units injected active power during an energization and load connection.

The system is energized and the load is connected at $t = 0.5$ seconds. In Fig. 1.5 the PCC voltage and the injected active power of each DG unit is shown. Observe that, due to the droop coefficients, the DG 2 injects the half of the power injected by DG 1. On the other hand, the controlled DG units could achieve a stable steady-state starting from zero and maintain stable after the load connection.

1.1.1.3 Grid-feeding control

Grid-feeding power converters are controlled as current sources; these power converters can be operated in parallel with other power converters. The references for this control are the active and reactive power, therefore, they are not able to operate in island mode if the voltage and frequency of the system are not adjusted, for example with a grid-forming power converter, or a local synchronous generator.

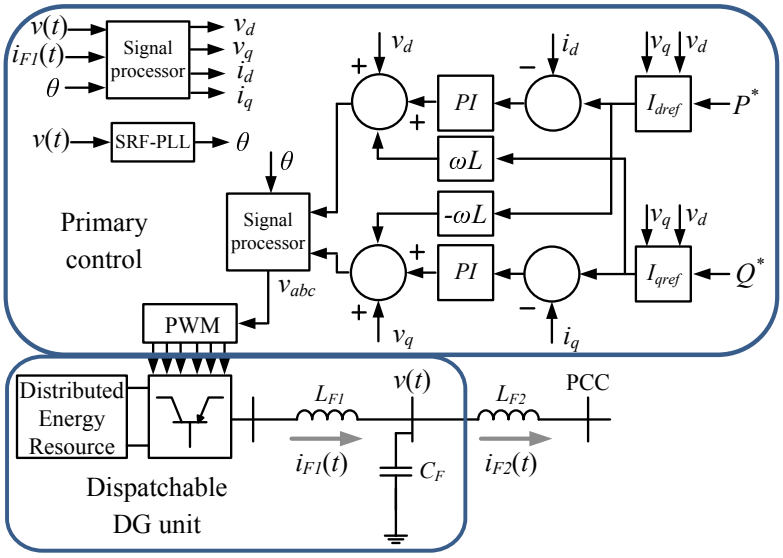

FIGURE 1.6: Basic grid-feeding control structure.

Figure 1.6 shows a basic grid-feeding structure, it includes a PLL to synchronize with the system and a current control loop. The active and reactive power references of the control are often set by a high level controller, such as an optimal power sharing. Note that in this controller, the dq current references I_{dref} and I_{qref}, are computed using the information of the power references and the dq voltage in the connection point as shown below,

$$I_{dref} = \frac{P^* v_d + Q^* v_q}{(3/2)(v_d^2 + v_q^2)} \tag{1.3}$$

$$I_{qref} = \frac{P^* v_q - Q^* v_d}{(3/2)(v_d^2 + v_q^2)} \tag{1.4}$$

where P^* and Q^* are the active and reactive power references, respectively, and v_d and v_q are the dq voltage measured in the filter capacitor.

A test case is presented below to show the grid-feeding control behavior. In Fig. 1.7 the single line diagram of the three-phase system is shown, it includes two DG units which are connected to the PCC. In this case, the system is connected to the main grid and after 6 cycles the DG units start working with active power references of 500 W and 300 W, for DG1 and DG2, respectively.

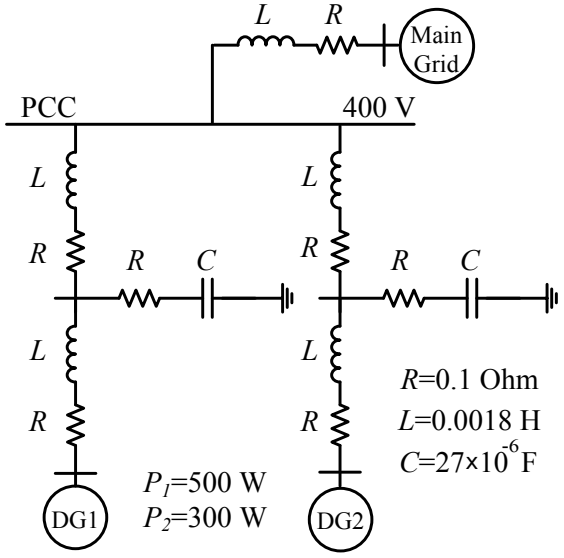

FIGURE 1.7: Single line diagram of the three-phase test system.

It can be seen in Fig. 1.8 the results in terms of the active power injected by each DG unit. Note that after the connection of the DG units, the power sharing achieves the steady-state in 0.18 seconds, following the active power references.

1.1.1.4 Proportional-resonant control

The proportional-resonant (PR) controller is a control that can be used for both, grid connected or islanded mode. This control scheme includes a proportional and a resonant term [17, 18],

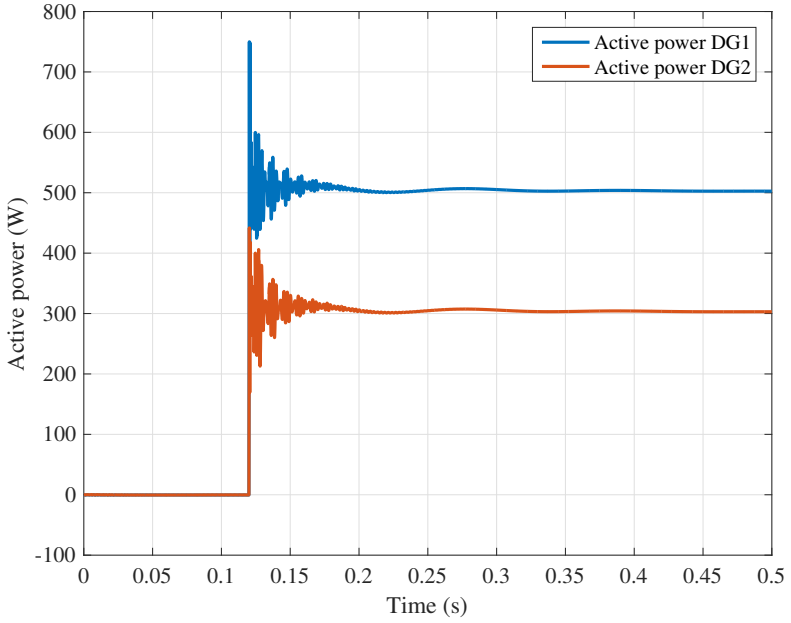

FIGURE 1.8: Injected active power by the DG units.

$$C_{PR}(s) = K_p + K_i \frac{s}{s^2 + \omega^2} \tag{1.5}$$

where ω is the resonant frequency, K_p the proportional gain and K_i the resonant gain. This control has a high gain around the resonant frequency such that the steady-state error when tracking or rejecting a sinusoidal signal is zero. Furthermore, in order to improve the performance, a harmonic compensator can be included and is given by [18],

$$C_{PRH}(s) = \sum_{h=1,2,3,\ldots} K_{ih} \frac{s}{s^2 + (\omega h)^2} \tag{1.6}$$

where h is the harmonic order and K_{ih} the harmonic resonant gain. It is worth noting that, the disadvantage of this scheme is that if the frequency of the system varies, the performance of the controller is degraded. In this way, if the system frequency varies significantly, adaptive mechanisms should be used. A PR controller is usually adopted in the stationary reference ($\alpha\beta$) frame for inverter control, therefore, only two voltages need to be controlled with two separate PR controllers. The block diagram of a voltage-controlled converter with the PR controller is shown in Fig. 1.9,

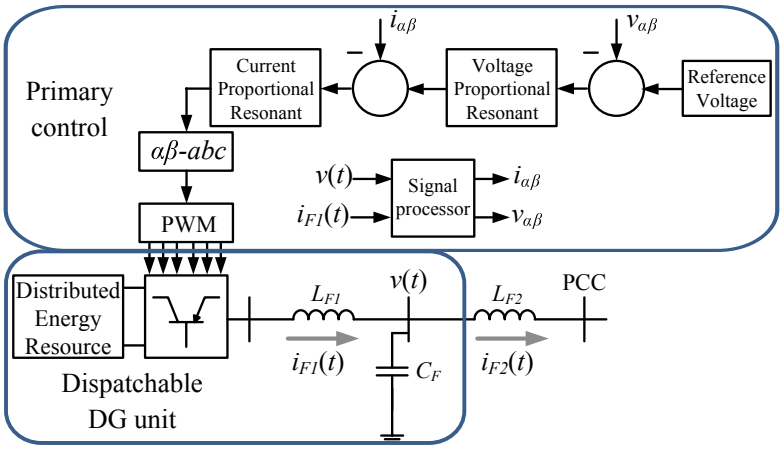

FIGURE 1.9: Basic proportional-resonant control structure.

If the controller is used as a current-controller, a PLL is needed to synchronize with the system. In the case of a voltage-controller the voltage reference could be made using a droop control as shown in Section 1.1.1.2. Finally, the outputs of the PR controllers are converted into PWM signals to drive the switches [18].

To shown the performance of the PR control, a case study is evaluated. The case study has the same electrical structure as Fig. 1.9, it includes a controlled DG unit, a LCL filter and a load connected to the PCC. The system parameters are shown in Table 1.1.

TABLE 1.1: Parameters of the case study microgrid and control

Parameter	Symbol	Value
Current loop proportional gain	k_{pc}	10
Current loop integral gain	k_{ic}	200
Voltage loop proportional gain	k_{pv}	1×10^{-2}
Voltage loop integral gain	k_{iv}	50
Fifth harmonic gain	k_{i5}	50
Seventh harmonic gain	k_{i7}	50
Eleventh harmonic gain	k_{i11}	250

The system is energized and the steady-state PCC voltage signals including a resistive load, a nonlinear load (diode bridge) and a nonlinear load but using harmonic rejection are shown in Figures 1.10(a), 1.10(b), and 1.10(c), respectively.

Note that, including only the resistive load, the voltage signals in the PCC do not have any harmonic distortion; however, when the nonlinear load is connected the signal get distorted with a THD of 3.51%. On the other side, including the harmonic rejection control for the 5^{th}, 7^{th} and 11^{th} harmonics, it can be seen in Fig. 1.10(c) that the harmonic content is reduced with a THD of 1.50%.

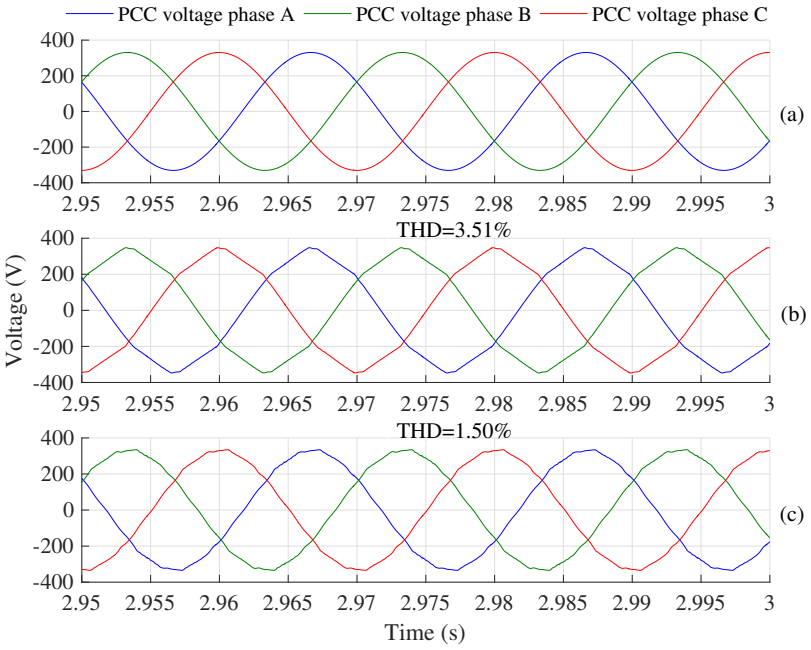

FIGURE 1.10: Basic proportional-resonant control performance.

1.1.2 AC microgrid secondary control

The secondary control level is responsible to compensate the MG frequency and voltage deviations [11], as shown in Fig. 1.11.

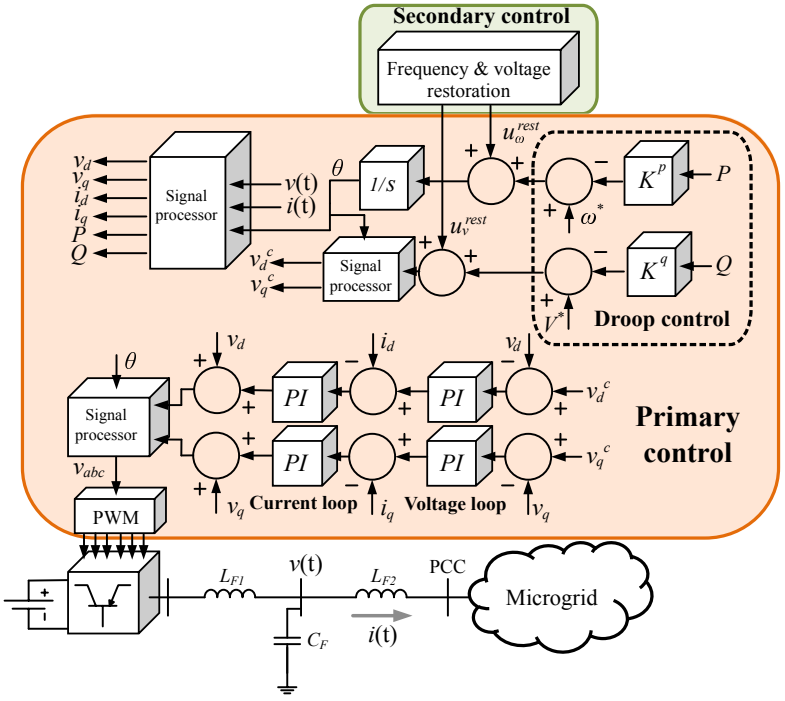

FIGURE 1.11: Hierarchical control block diagram.

This control measures the system frequency and bus voltage and compare them against the references ω^* and $|V_m^{**}|$, respectively. Keep in mind that, $|V_n^*|$ is the voltage reference for the primary control, while $|V_m^{**}|$ is the voltage reference for the secondary control. The error in each case of the secondary control is processed through a proportional-integral (PI) controller to obtain the output signals u_ω^{rest} and u_v^{rest}, as follows,

$$u_\omega^{rest} = k^{pw}(\omega^* - \omega_m) + k^{iw}\int(\omega^* - \omega_m)dt \tag{1.7}$$

$$u_v^{rest} = k^{pv}(|V_m^{**}| - |V_m|) + k^{iv}\int(|V_m^{**}| - |V_m|)dt \tag{1.8}$$

where ω_m and $|V_m|$ are the angular frequency and the voltage magnitude measured in the m-th bus, respectively. In this bus, the secondary control restores the frequency and voltage magnitude. It is important to mention that the secondary frequency control works using the SRF-PLL measurements, and these influence the DG units output phase.

The output signals u_ω^{rest} and u_v^{rest} are sent to each DG unit to restore the frequency and voltage deviations after every change in the microgrid, therefore, the equations (1.1) and (1.2) are modified as follows,

$$\omega_n = \omega^* - K_n^p P_n + u_\omega^{rest} \tag{1.9}$$

$$|V_n| = |V_n^*| - K_n^q Q_n + u_v^{rest} \tag{1.10}$$

It is worth mentioning that, in a microgrid with a point of common coupling (PCC), both frequency and voltage restoration controllers are controlling the same bus; however, in the case of a multi-bus microgrid, the voltage restoration control can be distributed in the different buses of the DG units [19].

1.2 Stability and resonance analysis of AC power electronics-based systems

In conventional power systems, stability analysis are well established with standard models of synchronous machines, governors and excitation systems of different orders

that are known to capture the necessary information for particular classes of problems [20]; however, the assumption of balanced and perfectly sinusoidal three-phase voltage and current waveforms are conditions increasingly difficult to sustain as valid in stressed and harmonic distorted scenarios, since harmonic generation, unbalance, interaction of control and harmonic components, resonances, etc, are phenomena commonly found in systems with high penetration of distributed generation units such as microgrids [21, 22].

Consequently, the stability analysis in electronics-based systems still have not reached the maturity, because their structure and control are relatively new. Furthermore, the fully interaction between power electronic-based DG units, the control and the system is still under research [23]. Therefore, this could result in practice, in erroneous or unfavorable operating scenarios overlooked in the design and evaluation stages [1, 20, 23].

In this way, stability and resonance issues that can be found in microgrids are analyzed using two case studies, which are presented below.

1.2.1 Case studies analysis

In this section two case studies are addressed, a controlled MG operating in islanded mode, and an open-loop system with three different transmission line models. The analyses are carried out with a detailed model (DM) that considers explicitly the commutation process of the power electronic devices, and a simplified model (SM) that considers only the fundamental frequency of the system. For the first case, the control is fully considered and includes a distributed droop-based power management strategy for each DG unit. In this case, the steady state is computed for both models (SM and DM) and the results are compared in terms of stability of the system. In the second case, the system energization is performed using a short line, PI line and distributed parameter transmission line models, the behavior of the transient and the steady-state are analyzed and the results obtained are compared.

1.2.1.1 Case I: Resonance effects on the asymptotic stability.

The microgrid used as test system is shown in Fig. 1.12. The system configuration and parameters were extracted from [24]. This system is operating in islanded mode and includes three voltage source converters based DG units with a modulation frequency (m_f) of 39, for interconnecting a primary source with the microgrid. Besides, in this case the transmission lines which interconnect the VSC's and the loads are modeled as a PI section line. The parameters of the case study are shown in Table 1.2.

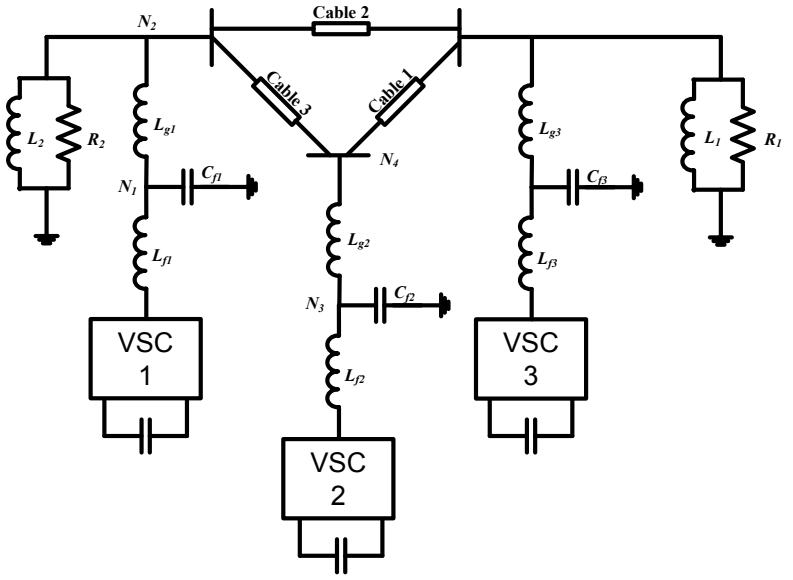

FIGURE 1.12: Single line diagram of the Case I, of a three-phase controlled microgrid.

TABLE 1.2: Parameters of the test system 1

Parameter	Symbol	Value
Filter inductance	L_{f1}, L_{f3}	12.7×10^{-3} H
Filter inductance	L_{g1}, L_{g2}, L_{g3}	1.48×10^{-3} H
Filter inductance	L_{f2}	1.27×10^{-3} H
Filter capacitance	C_{f1}, C_{f3}	3.97×10^{-6} F
Filter capacitance	C_{f2}	2.15×10^{-5} F
Lines inductance	Lin_L	2.12×10^{-4} H
Lines capacitance	Lin_C	3.31×10^{-6} F
Lines resistance	Lin_R	0.208 Ω
Inductance load	L_1, L_2	21.4×10^{-2} H
Resistance load	L_1, L_2	1.92 Ω

A droop control is used in order to perform a power management strategy (PMS) in the test system [25]. The PMS of the microgrid includes three main parts, the real power management, the reactive power management and the current controller.

The real and reactive power management blocks establish the real and reactive power outputs of each DG unit, respectively, based on the frequency and voltage at the connection point. The block of current controller takes the outputs of the real and reactive power blocks and generates the voltage reference of the controlled voltage source converter (VSC) [25]. It is worth mentioning that, due to the sinusoidal pulse width modulation (SPWM) used in the power converters, the first significant harmonic component that appear in the system is the $mf \pm 2$.

Figure 1.13 shows the voltages at the output filter of the VSC 1 with the SM and DM,

respectively; observe that using the SM, the MG reaches the steady state and remains stable (Fig. 1.13(a)); however, when the DM (m_f=39) is used, the harmonic content distorts the signal of voltage and also excites a near resonant frequency, causing in consequence, an instability of the MG, as it can be seen in the voltage signals at Fig. 1.13(b). The driving point impedance in different points of the MG are shown in Fig. 1.14; note that the resonance in N_1, with a peak in 2160 Hz, is the one that provokes the bad operation of the MG due to the first voltage harmonics injected by the inverter will be in $m_f \pm 2$. On the other hand, note that in this system, even with smaller or bigger switching frequency the MG could have resonance issues close to m_f=21 and m_f=150; in this way, in the design and planning stages of the microgrid is crucial to include detailed models, in order to avoid undesirable behaviors as is shown in this case study.

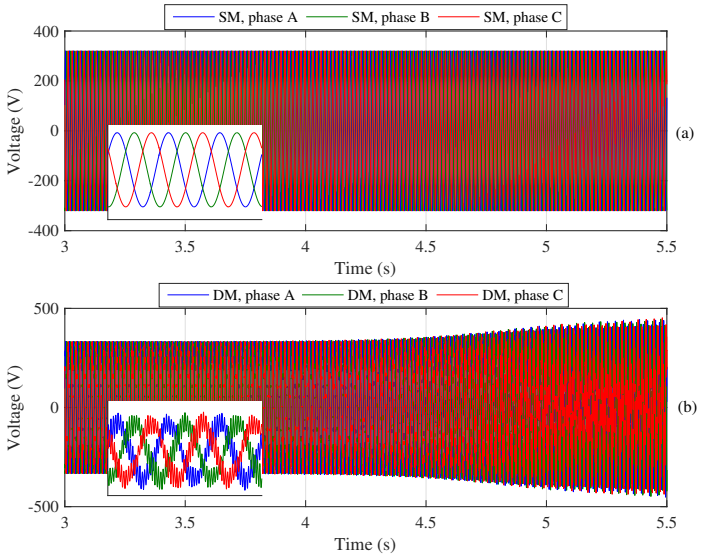

FIGURE 1.13: Voltages, (a) at the output of the VSC 1 filter with the SM, (b) at the output of the VSC 1 filter with the DM.

Being that the resonances appear due to the combination of capacitive and inductive elements, it is observed in Fig. 1.12 that the parallel resonances in this system are caused due to the filters, and transmission lines which in this case are modeled as equivalent PI lines. However, since this modeling approach of the transmission line use lumped parameters, it does not withhold the information of the high frequencies of the MG and, in consequence, resonance frequencies that exist in the real system and which can cause instabilities, are not taken into consideration. Nevertheless, if all the information wants to be retained, a model of distributed parameters of the transmission line is needed. In this regard, in the next case a comparison of the behavior of a system using different line models is analyzed.

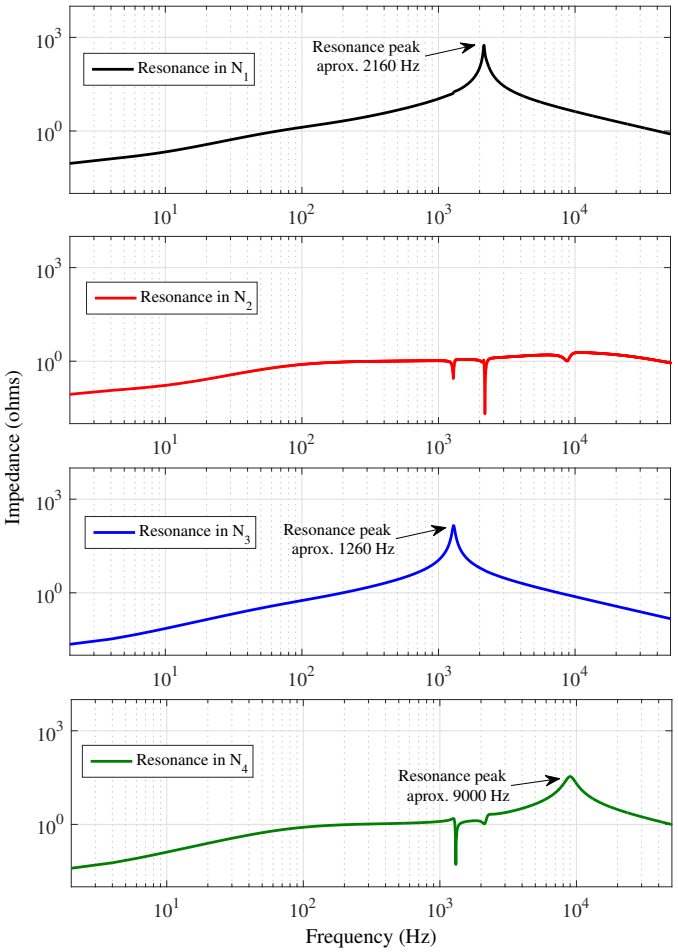

FIGURE 1.14: Resonance frequencies of the MG in Case I.

1.2.1.2 Case II: Behavior of a system with different transmission line models

Despite that microgrids do not have long transmission lines (hundreds of km), this case study is presented because they can operate connected to the main grid, and the main grid do have long transmission lines that can affect the behavior of the microgrid due to resonances as shown in this case study.

The single line diagram of a three-phase test system is shown in Fig. 1.15. It is composed by three transmission lines, two ideal feeders, and a VSC connected to an ideal DC voltage source. In this test system the energization of the system is performed and the computation of the transient and steady-state responses of the system is carried out using different transmission line models (short line, PI line and distributed parameters) for the SM and DM. It is worth mentioning that for the results obtained using the short line and PI line transmission models, only the integration of the state-space model of the system were needed; but, in order to obtain the results with the distributed parameters line model, the use of the numerical Laplace transform was required [26].

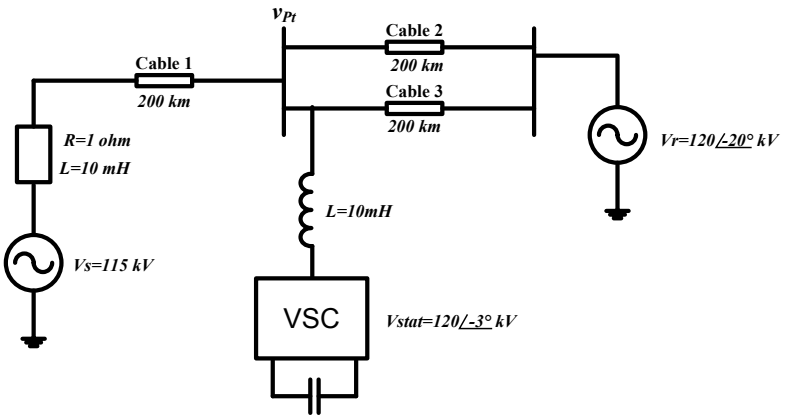

FIGURE 1.15: Single line diagram of the three-phase system in Case II.

Fundamental frequency. Figure 1.16 shows the transient and steady-state responses of the voltage at the bus v_{Pt}. Observe in Fig. 1.16(a) that using the frequency dependent model of the transmission line, the information of the traveling wave rebounds is kept, as well as, the increase of the voltage magnitude in the transient stage and the distortion of the waveforms. On the other hand, with the PI model the transient magnitude of the voltage is similar to the frequency dependent model but the voltage waveform is different as shown in Fig. 1.16(b). The short line model only captures the average of the voltage signal and the transient overvoltage is not captured (see Fig. 1.16(c)). Finally, in steady-state the three models have the same response, as it can be seen in Fig. 1.16(d), since for low frequencies, the characteristic impedance of the system is the same for the three line models, as shown in Fig. 1.18. Please notice that the short line model gives a maximum overshoot of 100 kV, while the PI line model and the full frequency dependent models have a maximum overshoot of 200 kV, which represents the double of the given by the short line model.

Switched case, $m_f = 153$. Figure 1.17 shows the transient and steady-state responses of the voltage at the bus v_{Pt}. In this case the transient responses using the frequency dependent line model and the PI line model are similar only in the maximum overshoot (see Fig. 1.17(a) and Fig. 1.17(b)). This is due the PI line model only keeps the low frequency information of the system dynamic, while the frequency dependent model preserves all the information of low and high frequencies. On the other hand, with the short line model, the voltage response is practically the switched voltage of the VSC (see Fig. 1.17(c)). Considering the PI line model, the voltage signal in steady-state presents a small harmonic content due to the system frequency characteristics; but, these are not equal to the resonances of the frequency dependent line model (see Fig. 1.18). This shows that the information given by the PI line model is not enough if detailed studies want to be carried out in systems with high-bandwidth. Additionally,

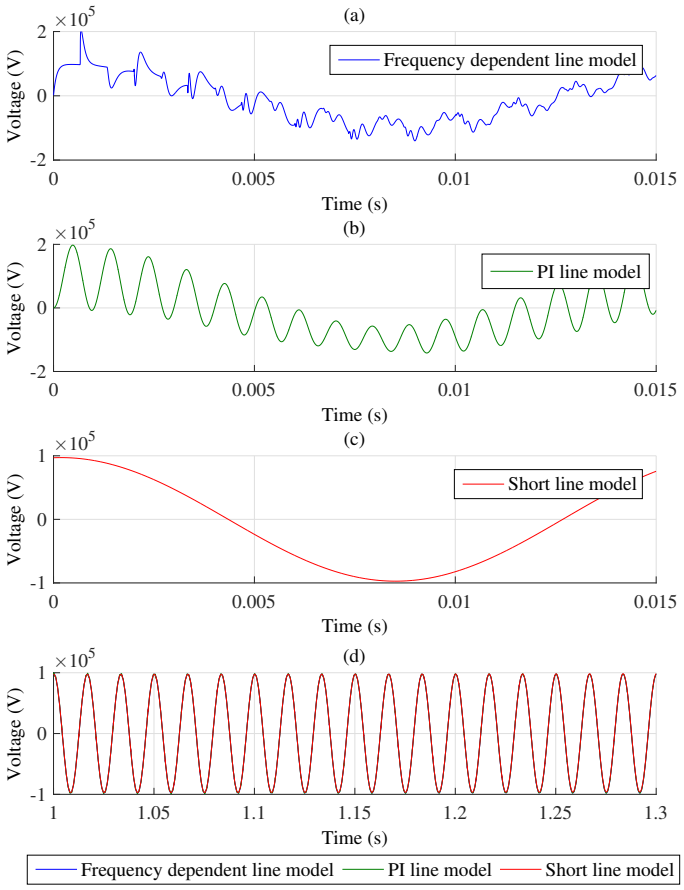

FIGURE 1.16: Transient response of the voltage at the bus v_{Pt} with, (a) the frequency dependent line model, (b) the Π line model, (c) the short line model; (d) the steady state response of the voltage at the bus v_{Pt} with the three line models.

with the short line model, the frequency characteristic behaves as a slope (see Fig. 1.18), this causes an erroneous increase in the voltage harmonic content as seen in Fig. 1.19. Therefore, the short line and PI line models are limited only to low frequency analyses, due to the phenomena of high frequencies is not correctly captured.

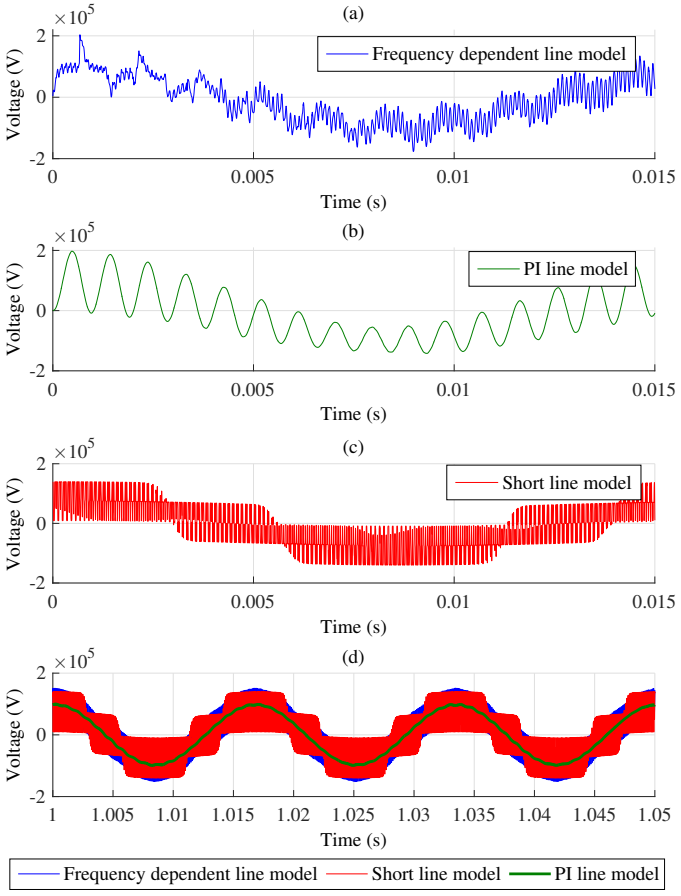

FIGURE 1.17: Switched case with $mf = 153$. Transient response of the voltage at the bus v_{Pt} with, (a) the frequency dependent line model, (b) the Π line model, (c) the short line model; (d) the steady state response of the voltage at the bus v_{Pt} with the three line models.

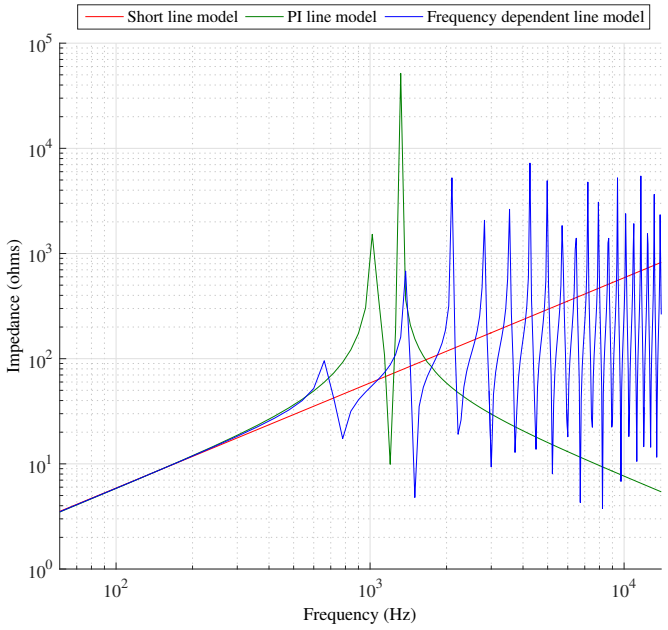

FIGURE 1.18: Driving point impedance seen from bus v_{Pt} with the three line models.

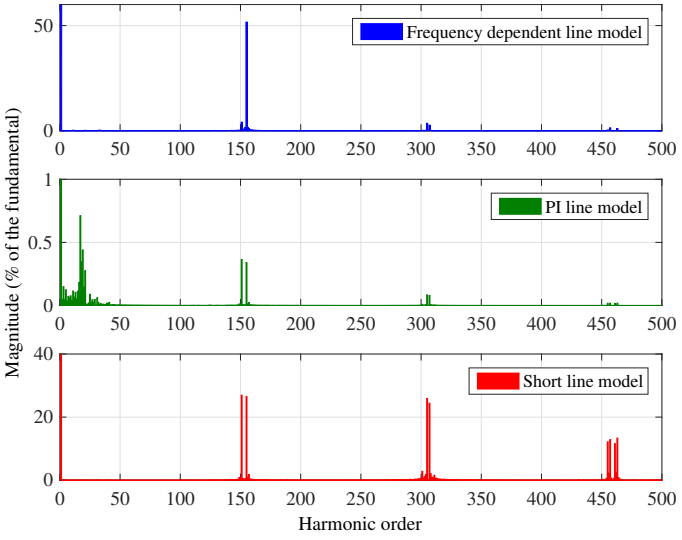

FIGURE 1.19: Voltage harmonic content at the bus v_{Pt} with the three line models, obtained using the Numerical Laplace Transform with 20 seconds of simulation.

1.3 Discussions

This chapter addressed the basic controls for AC microgrids, used to form hierarchical schemes, which maximize its reliability and potential benefits. The primary and secondary controls are explained in detail, and block diagrams of each control scheme are included. Additionally, to show the control schemes behavior, three case studies are analyzed.

On the other hand, to show the issues that can be found in practical AC microgrids, a stability and resonance analysis of two case studies was performed. It can be seen in the presented results that the commutation process of the power electronic interfaces has a significant effect in the microgrid behavior due to the harmonic components, resonances, and interaction among DG units.

The test systems revealed, as stated in the beginning of the chapter, that for stressed and/or harmonic distorted scenarios is necessary to consider the commutation process of the power electronic devices in order to not overlook phenomena or undesirable behaviors of the system. This leads to the necessity of developing theory, models and methods to identify and mitigate harmonic problems in power electronic based power systems, such as microgrids. In this regard, in the following chapter, different techniques for the fast computation of the periodic steady-state of controlled AC microgrids are addressed.

Chapter 2

Periodic steady-state computation of AC microgrids in time and frequency domains

In order to ensure the safe, reliable and controlled operation of a microgrid system, it is necessary to carry out model-based studies for design purposes, monitoring, control, network reconfiguration, etc. Some of these studies are carry out in transient state and others in steady state; nonetheless, for any of these scenarios, efficient mathematical models and computational algorithms for execution and analysis are needed. In particular, for the steady-state solution of an MG system is necessary to carry out studies such as power quality, stability, design of components, power flow, robustness, among others; however, despite that in conventional power systems the analysis previously mentioned are well established [20], during the design stage of the MG, the computation of the steady-state solution represents a challenging task due to the incorporation of power electronic converters, nonlinear loads and closed-loop control systems.

In regards of the aforementioned, this chapter addresses the formulation and performance assessment of different methods, in the time and frequency domains, to compute the steady-state solution of AC microgrids, such as, the Newton methods [27], Newton methods including parallel cloud computing and an extended power flow method.

2.1 Newton methods: a review

In general, the mathematical model of periodic switched nonlinear electric power systems can be given by the following ordinary differential equation set,

$$\dot{\mathbf{x}} = \mathbf{f}(t, \mathbf{x}) \tag{2.1}$$

where $\mathbf{x}$ is the state vector of n elements.

The periodic steady-state solution of (2.1) has a fundamental period T, such that the following relation is satisfied in steady state,

$$\mathbf{x}_T = \mathbf{x}_0 \tag{2.2}$$

where $\mathbf{x}_0$ is the state vector at t_0 and $\mathbf{x}_T$=$\mathbf{x}(t_0 + T,\ t_0;\ \mathbf{x}_0)$; for simplicity t_0 can be set equal to zero. Besides, the representation of dynamical periodic systems can be performed by using a Poincaré map $\mathbf{P}(\mathbf{x})$. Thereby, (2.2) can be written as follows,

$$\mathbf{x}_T = \mathbf{P}(\mathbf{x}_0) \tag{2.3}$$

Then, this problem can be solved through an iterative Newton method,

$$\mathbf{x}_0^{i+1} = \mathbf{x}_0^i - \left(\left. \frac{\partial \mathbf{P}(\mathbf{x}_0)}{\partial \mathbf{x}_0} \right|_{\mathbf{x}_0 = \mathbf{x}_0^i} - \mathbf{I} \right)^{-1} (\mathbf{P}(\mathbf{x}_0^i) - \mathbf{x}_0^i) \tag{2.4}$$

The periodic steady-state solution is found once two consecutive state vectors meet a convergence criterion error. Also, the state transition matrix $\mathbf{\Phi}$ can be defined as,

$$\mathbf{\Phi} = \left. \frac{\partial \mathbf{P}(\mathbf{x}_0)}{\partial \mathbf{x}_0} \right|_{\mathbf{x}_0 = \mathbf{x}_0^i} \tag{2.5}$$

which also can be approximated by finite differences as follows [28],

$$\mathbf{\Phi} \approx \left. \frac{\Delta \mathbf{x}_T}{\Delta \mathbf{x}} \right|_{\mathbf{x} = \mathbf{x}_0^i} \approx \left. \frac{\Delta \mathbf{P}(\mathbf{x})}{\Delta \mathbf{x}} \right|_{\mathbf{x} = \mathbf{x}_0^i} \tag{2.6}$$

It should be noticed that the eigenvalues of $\mathbf{\Phi}$ are the Floquet multipliers [28]; therefore, the transition matrix of the computed solution (2.4) can be used to obtain the stability of the periodic solution of the system [27], i.e. if all the Floquet multipliers are inside the unit circle in the complex plane Z the system is stable, otherwise unstable.

Several methods have been developed to compute $\mathbf{\Phi}$ [29], and all those methods rely on numerical integration processes. Each method differs from each other on how the approximation is done, and in the number of full cycles required for the full identification of $\mathbf{\Phi}$. In this way, a concise description of each methods is given below.

2.1.1 Aprille & Trick method

The Aprille & Trick (AT) method [30] starts using the following expression,

$$\frac{d}{dt}\mathbf{z}^i(t) = \mathbf{F}(t, \mathbf{x}_0^i)\mathbf{z}^i(t) \tag{2.7}$$

where,

$$\mathbf{z}^i(t) = \left.\frac{\partial \mathbf{x}(t)}{\partial \mathbf{x}_0}\right|_{\mathbf{x}_0=\mathbf{x}_0^i} \tag{2.8}$$

$$\mathbf{F}(t, \mathbf{x}_0^i) = \left.\frac{\partial \mathbf{f}(t, \mathbf{x})}{\partial \mathbf{x}_0}\right|_{\mathbf{x}_0=\mathbf{x}_0^i} \tag{2.9}$$

$\mathbf{F}(t, \mathbf{x}_0^i)$ is the Jacobian of $\mathbf{f}(t, \mathbf{x})$ evaluated along the trajectory $\mathbf{x}(t, t_0; \mathbf{x}_0^i)$ for $t_0 < t < t_0 + T$. The first step to develop the AT formulation is to select a numerical integration method. As example, the backward Euler method is considered and applied to (2.7),

$$\mathbf{z}^i(t_{m+1}) \approx \mathbf{z}^i(t_m) + \Delta t \mathbf{F}(t_{m+1}, \mathbf{x}(t_{m+1}))\mathbf{z}^i(t_{m+1}) \tag{2.10}$$

where Δt is the integration step, additionally, $t_0 = 0$, $t_m = m\Delta t$ for $m = 0, 1, 2, ..., K$, and $t_k = T$. Making some algebraic manipulations, (2.10) can be rewritten as,

$$\mathbf{z}^i(t_{m+1}) \approx [\mathbf{I} - \Delta t \mathbf{F}_{m+1}]^{-1}\mathbf{z}^i(t_m) \tag{2.11}$$

where $\mathbf{F}_{m+1} = \mathbf{F}(t_{m+1}, \mathbf{x}(t_{m+1}))$, therefore,

$$\mathbf{z}^i(t_k) \approx \mathbf{z}^i(T) \approx \prod_{m=1}^{K} [\mathbf{I} - \Delta t \mathbf{F}_{\mathbf{K}-m+1}]^{-1}\mathbf{z}^i(t_0) \tag{2.12}$$

According with (2.7)-(2.12), the transition matrix can be approximated as follows,

$$\Phi \approx \prod_{m=1}^{K} [\mathbf{I} - \Delta t \mathbf{F}_{\mathbf{K}-m+1}]^{-1} \tag{2.13}$$

In a similar manner, other approximations for the transition matrix can be done by using different numerical integration methods.

2.1.2 Numerical differentiation method

The numerical differentiation (ND) method [31], search a numerical approximation of $\Delta\mathbf{x}_T|_{\mathbf{x}=\mathbf{x}_0^i}$ and $\Delta\mathbf{x}|_{\mathbf{x}=\mathbf{x}_0^i}$ as follows,

$$\Delta\mathbf{x}|_{\mathbf{x}=\mathbf{x}_0^i} = \mathbf{x}(t_0, t_0; \mathbf{x}_0^i + \Delta\mathbf{x}_0^i) - \mathbf{x}(t_0, t_0; \mathbf{x}_0^i) \tag{2.14}$$

$$\Delta\mathbf{x}_T|_{\mathbf{x}=\mathbf{x}_0^i} = \mathbf{x}(t_0 + T, t_0; \mathbf{x}_0^i + \Delta\mathbf{x}_0^i) - \mathbf{x}(t_0 + T, t_0; \mathbf{x}_0^i) \tag{2.15}$$

If the perturbation vector $\Delta\mathbf{x}_0^i$ is selected as εU_k, being ε a small real number and U_k the k-th column of the identity matrix of size n, where $k = 1, 2, ..., n$, then (2.14) and (2.15) can be rewritten as follows,

$$\Delta\mathbf{x}|_{\mathbf{x}=\mathbf{x}_0^i} = \varepsilon U_k \tag{2.16}$$

$$\Delta\mathbf{x}_T|_{\mathbf{x}=\mathbf{x}_0^i} = \mathbf{P}(\mathbf{x}_0^i + \varepsilon U_k) - \mathbf{P}(\mathbf{x}_0^i) \tag{2.17}$$

Therefore, with (2.16) and (2.17), (2.6) becomes,

$$\mathbf{P}(\mathbf{x}_0^i + \varepsilon U_k) - \mathbf{P}(\mathbf{x}_0^i) \approx \mathbf{\Phi}\varepsilon U_k \tag{2.18}$$

where $\Phi_k = \mathbf{\Phi} U_k$ is the k-th column of $\mathbf{\Phi}$ and can be approximated as,

$$\Phi_k \approx \frac{\mathbf{P}(\mathbf{x}_0^i + \varepsilon U_k) - \mathbf{P}(\mathbf{x}_0^i)}{\varepsilon} \quad \forall\ k = 1, 2, ..., n \tag{2.19}$$

Each column of $\mathbf{\Phi}$ is computed using (2.19). The n states of (2.1) have to be perturbed separately to compute the n columns of the transition matrix. Note that $n+1$ full cycles have to be computed before (2.4) can be applied.

2.1.3 Direct approximation method

The direct approximation (AD) method [31] is based on the computation of the linearized version of (2.1) around the orbit initiated in $\mathbf{x}_0^i$, this is,

$$\Delta\dot{\mathbf{x}}(t) = \mathbf{F}(t, \mathbf{x}_0^i)\Delta\mathbf{x}(t) \tag{2.20}$$

The solution of (2.20) is,

$$\Delta\mathbf{x}(t) = \mathbf{\Phi}(t, t_0; \mathbf{x}_0^i)\Delta\mathbf{x}(t_0) \tag{2.21}$$

Besides,

$$\Delta\mathbf{x}(t_0) = \Delta\mathbf{x}|_{\mathbf{x}=\mathbf{x}_0^i} \tag{2.22}$$

$$\Delta\mathbf{x}(t_0 + T) = \Delta\mathbf{x}_T|_{\mathbf{x}=\mathbf{x}_0^i} \tag{2.23}$$

According with (2.21) to (2.23),

$$\Delta\mathbf{x}_T|_{\mathbf{x}=\mathbf{x}_0^i} = \mathbf{\Phi}\ \Delta\mathbf{x}|_{\mathbf{x}=\mathbf{x}_0^i} \tag{2.24}$$

If the perturbation vector is selected as U_k, then (2.24) becomes,

$$\Delta\mathbf{x}_T|_{\mathbf{x}=\mathbf{x}_0^i} = \mathbf{\Phi}U_k = \Phi_k \tag{2.25}$$

Therefore, this AD method is an approximated way to compute $\mathbf{\Phi}$, since $\Delta\mathbf{x}_T|_{\mathbf{x}=\mathbf{x}_0^i}$ is approximated as $\Delta\mathbf{x}(t_o + T)$, which is the numerical solution of (2.20).

2.1.4 Enhanced numerical differentiation method

The enhanced numerical differentiation (END) method [32] takes advantage of the half-wave symmetry of the input waveforms, such as voltage and current, to improve the efficiency of the ND method. This method consist in the evaluation of (2.6) with the approximation of $\mathbf{x}(t_0 + T, t_0; \mathbf{x}_0^i)$ through the extrapolation of $\mathbf{x}(t_0 + T/2, t_0; \mathbf{x}_0^i)$.

Using this method, the integration of (2.1) for the computation of $\mathbf{\Phi}$, it is done in $T/2$ instead of T, which increases the efficiency of the ND method. In this way, the integration of (2.1) is needed for $(n + 1)/2$ full cycles to complete the computation of the transition matrix for each Newton iteration.

2.1.5 Discrete exponential expansion method

In the discrete exponential expansion (DEE) method [33], the transition matrix $\mathbf{\Phi}$ is obtained following a procedure of identification step-by-step based in a recursive formulation. The identification of $\mathbf{\Phi}$ requires the integration of only one full cycle of period T. In this method the approximation is carried-out as follows,

$$\mathbf{\Phi} \approx \prod_{m=1}^{K} e^{\mathbf{F}_m \Delta t_m} \tag{2.26}$$

the Jacobian matrix $\mathbf{F}_m$ is,

$$\mathbf{F}_m = \mathbf{F}(t, x(t))\big|_{t=\frac{t_m+t_{m-1}}{2}, x=\frac{x(t_m)+x(t_{m-1})}{2}} \tag{2.27}$$

where Δt_m is defined as $t_m - t_{m-1}$, K is the number of intervals in a period T, and t_m is the m-th element of the time vector from t_0 to $t_0 + T$.

2.1.6 Finite differences method

The finite differences (FD) method [27] is an alternative in the time domain for the fast computation of the periodic steady-state solution of (2.1). The problem in this method is formulated as a set of nonlinear differential equations. The method is applied in two steps:

- Select a fix-step numerical integration method. Select an integer $K > 0$ such that $\Delta t = T/K$ and $t\epsilon(t_0, t_1, ..., t_k)$, where $t_m = t_0 + m\Delta t$ for $m = 0, 1, 2, ..., K$.
- Let $\mathbf{x}_m = \mathbf{x}(t_m, t_{m-1}; \mathbf{x}_{m-1})$, then the sequence of $\mathbf{x}_m$ approximates the steady-state solution if $\mathbf{x}_0 = \mathbf{x}_K$ and $\mathbf{x}_m = \mathbf{x}(t_m, t_{m-1}; \mathbf{x}_{m-1})$ for $m = 0, 1, 2, ..., K$. Each state vector of $\mathbf{x}_m$ is obtained with the selected integration method. Once the K equations are set, the Newton method is applied.

For the implementation of this method large matrices have to be handled, therefore, disperse matrices techniques can be applied.

2.2 Newton methods performance assessment

Figure 2.1 shows the single line diagram of the microgrid used as test system. Its mathematical model including the control system has 86 ordinary differential equations for grid-connected mode and 83 for islanded mode. The system configuration, parameters and control scheme were extracted from [25, 34]. The MG has a nominal voltage of 13.8 kV and it is connected through a transformer to a harmonic free infinite bus (main grid) of 69 kV. The three distributed generation units include a voltage source converter [35] with a RL filter of $0.01 + j0.15$ $p.u.$ and a frequency modulation index (m_f) of 21 (1260 Hz). Note in Fig. 2.1 that the branches of the microgrid are represented as equivalent impedances, furthermore, the loads are included in the impedances for the case of branches with PQ loads.

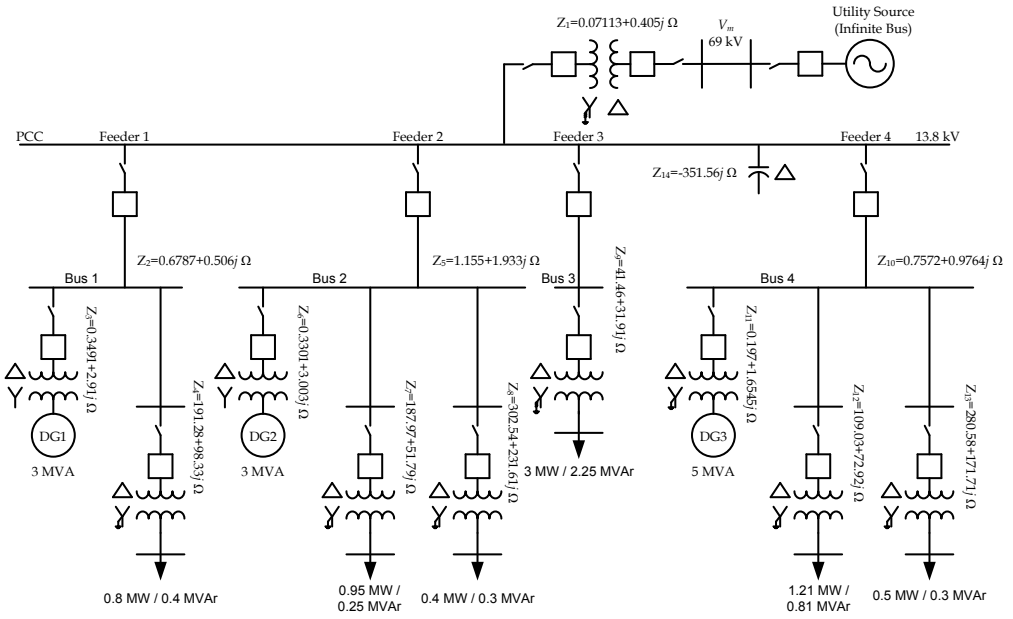

FIGURE 2.1: Single line diagram of the test system microgrid.

In this case, the microgrid is interconnected to the main grid operating in periodic steady state, when is suddenly disconnected to operate in islanded mode. The accelerated computation of periodic solution for the case study is carried out with the six Newton methods aforementioned (DEE, AT, FD, DA, ND and END), and the results obtained are compared to assess the advantages and disadvantages of each method. The convergence error tolerance used in the case study is 1×10^{-8} and the state vector at the end of the 10^{th} cycle is used for initialization of the Newton methods; the computation of this state vector is performed through numerical integration of (2.1) using as initial condition the state vector at $t = 0$ of the previous operating conditions in steady state, i.e., grid-connected mode for the case study. After the 10^{th} cycle the Newton iterations begin and the convergence mismatches are given in multiples of the cycles that each method

needs to iterate, i.e., DEE, AT and FD methods require one full cycle, the ND and DA methods require $(n+1)$ cycles and the END method requires $(n+1)/2$ cycles, where n is the number of ordinary differential equations of the system model.

Table 2.1 shows the results obtained in terms of the number of cycles required to obtain the periodic steady-state solution and the Newton iterations are highlighted in gray. Observe in Table 2.1 that the BF method requires 5283 full cycles and reaches the periodic steady state with an error of 9.978×10^{-9}, while the DEE method requires 5 Newton iterations and the others methods require 3 Newton iterations. The END, DA, AT, ND, and FD methods have a quadratic convergence characteristic. Although the DEE method requires more iterations is also the fastest since the time to compute the transition matrix at each Newton iteration is less as compared with the others Newton methods.

Table 2.2 shows the relative efficiency of each method respect to the BF method to achieve the periodic steady-state solution within the established tolerance. Besides, the maximum Floquet multiplier is calculated for each method. Notice that $\mathbf{\Phi}$ is not computed in the BF and FD methods, therefore the Floquet multipliers cannot be calculated with those methods and neither the stability of the computed periodic solution; however, in this case, it is clear that the periodic steady-state solution is stable since the BF method is able to reach it. Additionally, it can be seen in Table 2.2 that the BF and DEE are the slowest and the fastest methods, respectively. DEE is around 68, 3.46, 3.46, 1.85, 1.83, and 1.79 times faster than BF, ND, FD, DA, AT and END, respectively. Observe that the maximum Floquet multiplier with each method (AT, ND, DA, END, and DEE) is computed and its value is inside the unit circle for all methods with standard deviation of 5.0438×10^{-4}.

From this comparison it can be seen that the Newton methods offer a suitable alternative to compute the periodic steady state solution of dynamical systems represented by full-order models. Additionally, they provide information about the asymptotic stability of the computed periodic steady state solution, except the FD method. Keep in mind that the six Newton methods are able to compute both stable and unstable periodic steady-state solutions, this is a valuable feature since the unstable solution can become stable with the proper selection of the control gains or system parameters.

TABLE 2.1: Mismatches during convergence of the methods in the case study

Cycles	BF	DEE	AT	FD	DA	ND	END
1	5.217×10^{-3}	5.217×10^{-3}	5.217×10^{-3}	5.217×10^{-3}	5.217×10^{-3}	5.217×10^{-3}	5.217×10^{-3}
2	6.226×10^{-3}	6.226×10^{-3}	6.226×10^{-3}	6.226×10^{-3}	6.226×10^{-3}	6.226×10^{-3}	6.226×10^{-3}
⋮	⋮	⋮	⋮	⋮	⋮	⋮	⋮
10	3.969×10^{-3}	3.969×10^{-3}	3.969×10^{-3}	3.969×10^{-3}	3.969×10^{-3}	3.969×10^{-3}	3.969×10^{-3}
11	3.843×10^{-3}	5.586×10^{-4}	2.224×10^{-5}	2.277×10^{-5}	⋮	⋮	⋮
12	3.729×10^{-3}	4.194×10^{-5}	5.594×10^{-8}	4.968×10^{-8}	⋮	⋮	⋮
13	3.623×10^{-3}	2.239×10^{-6}	5.465×10^{-12}	1.567×10^{-12}	⋮	⋮	⋮
14	3.524×10^{-3}	5.745×10^{-8}			⋮	⋮	⋮
15	3.431×10^{-3}	5.316×10^{-9}			⋮	⋮	⋮
⋮	⋮				⋮	⋮	⋮
52	1.502×10^{-3}				⋮	⋮	3.290×10^{-5}
⋮	⋮				⋮	⋮	⋮
94	1.100×10^{-3}				2.224×10^{-5}	2.309×10^{-5}	2.662×10^{-8}
⋮	⋮				⋮	⋮	⋮
136	2.110×10^{-3}				⋮	⋮	2.604×10^{-12}
⋮	⋮				⋮	⋮	
178	1.207×10^{-3}				5.538×10^{-8}	4.660×10^{-8}	
⋮	⋮				⋮	⋮	
262	5.484×10^{-4}				5.338×10^{-12}	5.479×10^{-12}	
⋮	⋮						
5283	9.978×10^{-9}						

TABLE 2.2: Comparison between CPU times and stability

Methods	CPU times (s)	Comparison between CPU times $\frac{T_{FB}}{T_{xx}}\|_{xx=FB,...,EED}$	Max. Floquet multiplier
BF	80007.10	1.00	N/A
ND	4056.70	19.72	0.9978
FD	4051.06	19.74	N/A
DA	2174.96	36.78	0.9978
AT	2152.25	37.17	0.9978
END	2094.94	38.19	0.9989
DEE	1169.95	68.38	0.9974

2.3 Newton methods implementation using parallel cloud computing

The advantages of using the Newton methods for the steady-state computation of electrical networks can be eclipsed for large and/or stiff systems. This is because the computational burden increases, and the computing time needed to solve the methods becomes a drawback.

An alternative to reduce the computational time spent by the Newton methods is the use of parallel cloud processing. Cloud computing can be defined as an environment where computing-needs from an user can be outsourced by an external provider, and all the services are provided through internet. One of the main advantages of this scheme is that users do not have to pay for infrastructure, installation, maintenance, among others, all is covered by the provider. On the other hand, apart from reducing the computation time of the Newton methods, a benefit of the parallel cloud computing scheme is the possibility to solve electric networks with a high number of components and without the limitation in the number of processors available in a single computer or a computer center. Fig. 2.2 shows the scheme used for parallel cloud computing.

2.3.1 Parallel cloud computing of Newton methods

Newton methods require the transition matrix construction which is one of the most time-consuming tasks, since it depends on the system equations number and it relies on numerical integration processes. However, the transition matrix can be obtained using parallel processing, reducing in this way the computing time. In this approach, the transition matrix is approximated by creating individual tasks which do not need the information one of each other.

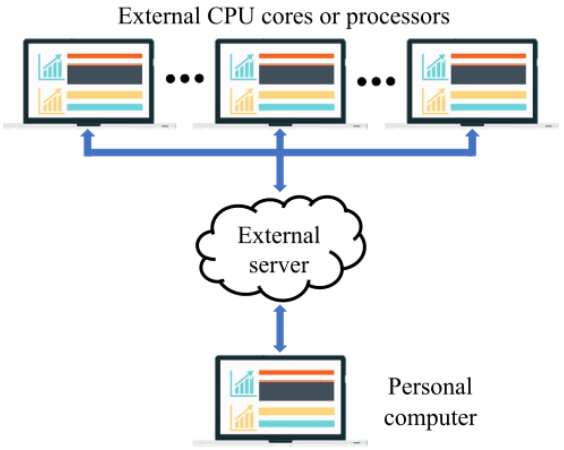

FIGURE 2.2: Parallel cloud computing scheme.

As can be seen from (2.19), in the ND and END methods, the transition matrix approximation is computed column by column, and the information needed to compute each column is independent from the others. Besides, in the DEE method, (2.26) shows that the transition matrix is computed by means of the multiplication of matrices, but each matrix is independent from each other. These characteristics bring the opportunity to take advantage of the ability to parallelize these numerical methods, in particular, for the computation of the transition matrix.

In this regard, the parallel computing toolbox of MATLAB can be used to parallelize the Newton method algorithms (ND, END, DEE) by splitting the transition matrix computation among CPU cores or processors. To perform the parallelization, the *parfor* command of MATLAB is used, this command splits the execution of *for-loop* iterations over the CPU cores, also known as "workers", in a parallel pool. Additionally, an important requirement for using *parfor-loops* is that individual iterations must be independent.

On the other hand, cloud computing services can be used together with the parallel computing toolbox of MATLAB. Cloud servers provide CPU cores required by the user and performs the simulation in the same MATLAB environment. This advantage eases the use of these advanced computing tools, since the user do not need to have physically the hardware required for the parallel implementation, i.e. multiple CPU cores, instead the user can use external CPU cores and run the simulations in the same MATLAB environment [36]. Fig. 2.3 shows the flowchart used to parallelize the Newton methods using the parallel computing toolbox of MATLAB and cloud computing.

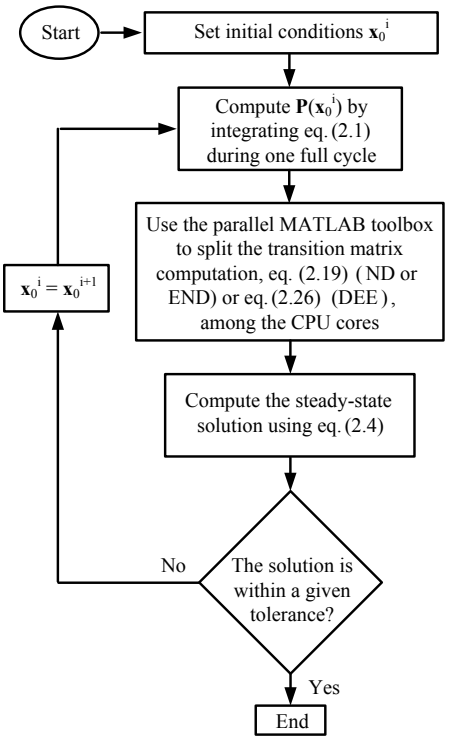

FIGURE 2.3: Flowchart of the Newton methods with parallel computing.

2.4 Newton methods parallel cloud computing performance assessment

Two test systems are implemented to assess the CPU time efficiency of the three fast time-domain methods (ND, END, DEE) using parallel cloud computing. The convergence error tolerance used in the case studies is 1×10^{-8}.

The parallel cloud computing was done through SSH connection with an external computer located in the Aalborg University. The specs of the external computer are: 2 Intel(R) Xeon(R) CPU E5-2690 v3 at 2.60GHz, 384 GB DDR4 memory RAM at 2133MHz, and 24 CPU cores.

2.4.1 Case I: controlled microgrid system

Fig. 2.4 shows the single line diagram of the microgrid used as test system. The system is composed by three distributed generation (DG) units, each one includes a VSC [35] with a modulation index (m_f) of 21, for interconnecting a primary source with the microgrid. The VSC controls used are based on a droop-characteristic scheme with frequency restoration [25]. This test system is modeled with 86 ordinary differential equations. The system configuration and parameters can be consulted in [25, 34].

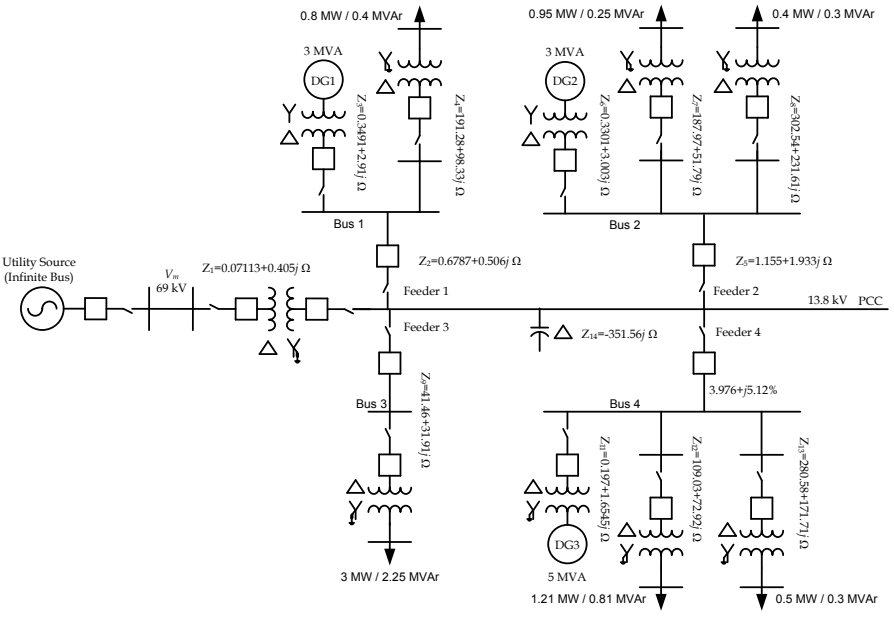

FIGURE 2.4: Single line diagram of the test system.

In this first case study, the microgrid is operating in steady state, then a perturbation is applied in the state variables of the system, varying their values in 5%, after that, the computation of the periodic steady-state solution is carried out using the Newton methods. The computation of the steady state is obtained several times, varying the number of CPU cores used to compare their relative efficiencies.

In Table 2.3 the convergence errors of the Newton methods for this case study are shown. Note that only two iterations are needed to achieve an steady-state solution, with an error in the order of 1×10^{-9}. Furthermore, in Fig. 2.5 is shown three full cycles of the currents obtained for the DG unit 1 after the application of the Newton methods, where it can be noticed that the periodic steady state is reached even in presence of harmonic distortion.

TABLE 2.3: Convergence errors of Case I

Iteration	DEE	ND	END
1	1.73×10^{-4}	1.72×10^{-4}	8.32×10^{-5}
2	7.81×10^{-9}	7.43×10^{-9}	5.98×10^{-9}

Fig. 2.6 shows the relative efficiency and CPU time required by the Newton methods in the computation of the steady-state solution, as the number of CPU cores increases. It is observed that the relative efficiency for the three methods increases up approximately to the 12th core, then the relative efficiency behavior flattens with small improvements until the 24th core. The best performance regarding the relative efficiency is obtained

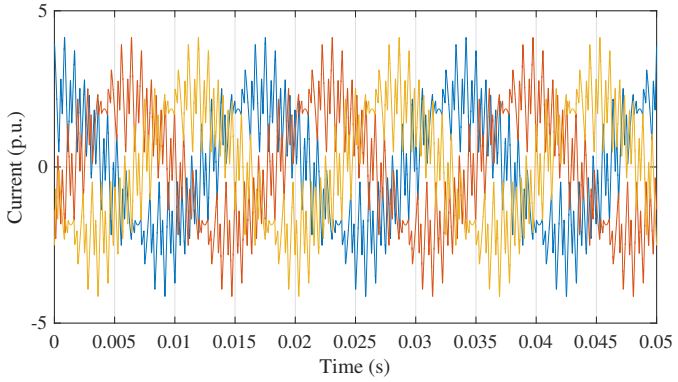

FIGURE 2.5: DG unit 1 output currents of the controlled microgrid system.

with the ND method, with an improvement of almost 9.73 times in its efficiency, followed closely by the END method with a relative efficiency of 8.6, and finally, the DEE method with a relative efficiency of 7.39, having the worst performance of the three methods. In regard to the CPU time, the DEE method requires only 39.28 seconds to obtain the solution, while the ND and END methods require 100.3 seconds and 52.94 seconds, respectively, using 24 CPU cores. Note that contrary to the relative efficiency results, the DEE method has the best CPU time performance, and the ND method the worst.

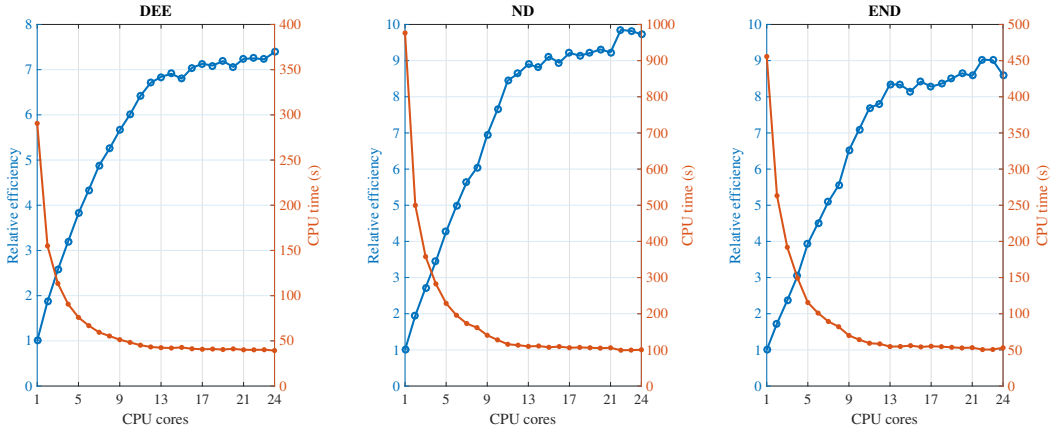

FIGURE 2.6: Relative efficiency and CPU time required by the Newton methods in Case I.

2.4.2 Case II: IEEE 118-bus test system

Although this system is not a microgrid, it is included to show the performance of the Newton methods using parallel cloud computing for larger systems. Besides, more complex MGs can require hundreds of ordinary differential equations to model them,

but there are not benchmarks for large microgrid systems, so the IEEE 118-bus system is used instead.

In this case, the IEEE test system of 118 nodes is used, it consists in 186 transmission lines, 118 capacitor banks, 54 generators and 9 magnetizing branches. The system is simulated from its start-up, and one full-cycle after this, it is computed the periodic steady-state solution with the Newton methods. This test system is modeled with 355 ordinary differential equations.

Table 2.4 shows the convergence errors of the methods in this case study. It is observed that the DEE method requires 5 iterations to achieve the steady state with an error of 1.66×10^{-9}, while the ND and END methods require 2 iterations with errors of 2.17×10^{-14} and 1.47×10^{-14}, respectively. Fig. 2.7 shows three full cycles of the current, in the obtainment of the steady-state solution, at different transmission lines of the test system.

TABLE 2.4: Convergence errors of the Case II

Iteration	DEE	ND	END
1	1.73×10^{-3}	1.44×10^{-8}	1.25×10^{-8}
2	4.00×10^{-5}	2.17×10^{-14}	1.47×10^{-14}
3	1.26×10^{-6}	-	-
4	4.44×10^{-8}	-	-
5	1.66×10^{-9}	-	-

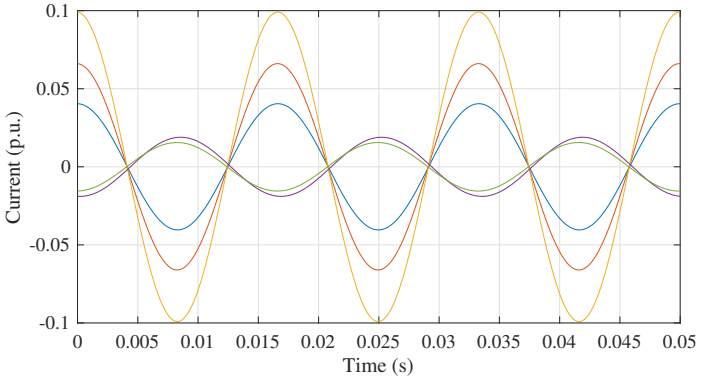

FIGURE 2.7: Steady-state currents at the transmission lines of the IEEE 118-bus benchmark.

The results obtained in this case study in terms of relative efficiency and CPU time required by the Newton methods are shown in Fig. 2.8.

From this figure, it can be seen that due to the size of the test system, even with the 24 CPU cores the relative efficiency is increasing. However, it is also observed that

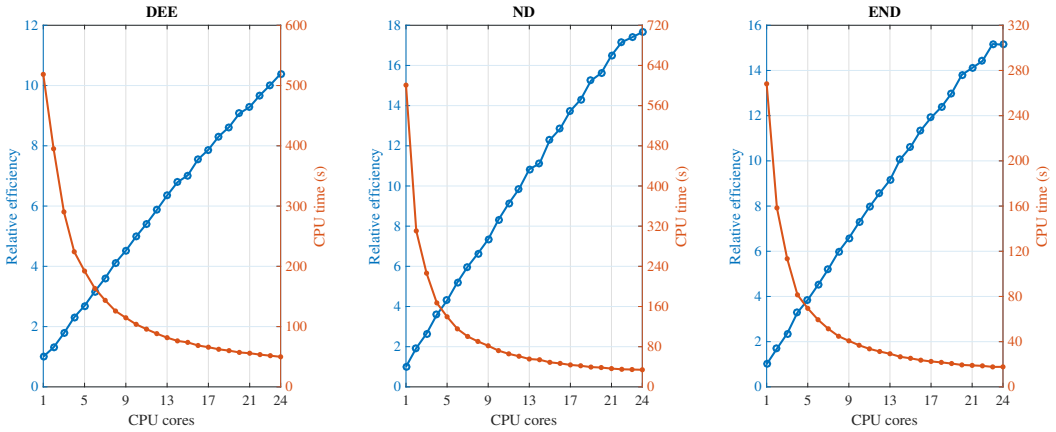

FIGURE 2.8: Relative efficiency and CPU time required by the Newton methods in Case II.

the CPU time graph is getting flat, therefore, despite that the methods achieve better relative efficiencies, the CPU time needed will be similar using more CPU cores. This behavior is due the communication time between cores and other aspects associated with the parallelization of the methods.

In this case the DEE, ND and END methods achieve relative efficiencies of 10.39, 17.66 and 15.14, respectively. Where the ND method has the best relative efficiency and the DEE method the worst. Regarding the CPU time, the DEE, ND and END methods achieve the steady-state solution in 49.86 seconds, 34.02 seconds and 17.71 seconds, respectively.

The results obtained in both case studies show the advantages of using parallel processing through cloud computing. Besides, the Newton methods are adequate to be parallelized. In the case of this work, with 24 CPU cores, in both cases the best relative efficiency obtained was 17.66 (Case II), and the worst 7.39 (Case I). Additionally, it is observed that in Case I, despite that the DEE method has the lower increase in the relative efficiency, it was the quickest method; however, for the Case II, it needed more CPU time than the ND and END methods. Therefore, this finding indicates that for large systems the ND and END methods are more efficient.

2.5 Power flow modeling for AC microgrids

In electric power systems, the power flow (PF) formulation relies on the well-known power balance equations [37],

$$P_n = \sum_{m=1}^{N} |V_n||V_m||Y_{nm}|cos(\theta_{nm} - \delta_n + \delta_m) \quad for\ n = 1, ..., N \tag{2.28}$$

$$Q_n = -\sum_{m=1}^{N} |V_n||V_m||Y_{nm}|sin(\theta_{nm} - \delta_n + \delta_m) \quad for\ n = 1, ..., N \tag{2.29}$$

where $|V_n|$, $|V_m|$, δ_n and δ_m are the magnitudes and phase angles of the n-th and m-th bus voltages, respectively. $|Y_{nm}|$ and θ_{nm} are the magnitude and phase angle of the admittance matrix elements, respectively.

Depending on the topology of the system, the power flow can be formulated using three types of buses: voltage-controlled (PV), load (PQ) and slack [38]. In this way, the active power injected to the system by the PV buses is fixed and known, while the slack bus provides the missing active and reactive power needed by the system. However, as compared with synchronous generators in conventional power systems, the injected active and reactive power by the distributed generation (DG) units in microgrids are not usually known at the starting of the Newton iterations since they depend on their specific control systems [1, 10, 11]. Therefore, a different power flow modeling of the DG units have to be addressed.

2.5.1 Droop-based extended power flow

In islanded droop controlled microgrids, the conventional power flow approach cannot be used in most of the cases because the following reasons [4, 39]: 1) the DG units used in a microgrid have a limited capacity, therefore, a slack bus cannot be assigned for all the operating conditions; 2) the active and reactive power sharing among the DG units depends on the droop characteristics and cannot be pre-specified such as in the conventional power flow; 3) the frequency in an islanded microgrid is changing constantly within a range, while in the conventional power flow, it is considered always fixed.

Despite that the slack bus could be reassigned or distributed in an islanded situation, the DG unit selected as slack bus should be able to provide all the missing active and reactive

power, but it could not always be possible due to their limited and not dispatchable capacity [4, 39].

In regard to the aforementioned, an extra bus classification has to be included to take into account the droop controlled DG units, hereafter called droop buses (DB) [39]. The DB formulation relies on the droop characteristic equations (1.1) and (1.2), notice that from these equations, the active and reactive power given by the n-th DG unit can be defined as,

$$P_n = \frac{\omega^* - \omega}{K_n^p} \tag{2.30}$$

$$Q_n = \frac{V_n^* - |V_n|}{K_n^q} \tag{2.31}$$

therefore, the mismatching equations ΔP_n and ΔQ_n for the n-th DG unit become,

$$\begin{bmatrix} \Delta P_n \\ \Delta Q_n \end{bmatrix} = \begin{bmatrix} P_n - (\frac{\omega^* - \omega}{K_n^p}) \\ Q_n - (\frac{V_n^* - |V_n|}{K_n^q}) \end{bmatrix} \tag{2.32}$$

Observe that, in (2.32) the angular frequency is still unknown, therefore, an extra equation related to it has to be included. To overcome this problem, one voltage angle of the DG units is fixed and its active power equation is used as the angular frequency equation as follows [40],

$$\begin{bmatrix} \Delta P_n \\ \Delta Q_n \\ \Delta \omega \end{bmatrix} = \begin{bmatrix} P_n - (\frac{\omega^* - \omega}{K_n^p}) \\ Q_n - (\frac{V_n^* - |V_n|}{K_n^q}) \\ K_n^p P_m - (\omega^* - \omega) \end{bmatrix} \tag{2.33}$$

where P_m is the active power of the fixed angle bus.

The set of mismatching equations given in (2.33) completes the power flow formulation of the droop buses, which can be used together with the conventional PV and PQ buses [39]. Note that this power flow model includes the effect of the basic primary droop control of DG units, however, practical microgrids require the use of hierarchical control schemes to achieve an optimal operation, accordingly, this problem is addressed in the following section.

2.5.2 Hierarchical extended power flow

Microgrids control requirements and strategies to perform local balancing and to maximize their benefits have led the MGs to fulfill a wide range of functionalities, such as power flow control to avoid exceeding line capacities, voltage and frequency regulation, energy balance, among others [11, 41–44]. In this way, practical MGs include hierarchical control schemes to achieve the desired operational requirements. Consequently, since the hierarchical controls modify the steady-state operation of the MG, they have to be included in the methods for the computation of the steady-state. Hierarchical control systems increase the difficulty of the power flow modeling since their secondary and tertiary controls change the operating points of the MGs, such that, the active and reactive power injected by the DG units differ from those injected by DG units with only droop control. Keep in mind that the tertiary control level typically operates in the order of minutes [1]. Therefore, their outputs can be considered constant in the power flow modeling; however, the operation time of the secondary control, such as the frequency and voltage restoration control, is close to the primary control operation time. Hence, the outputs of the secondary control cannot be assumed as constant inputs to the primary control. For these reasons, the power flow model must include primary and secondary controllers.

As mentioned before, the power flow formulation for islanded microgrids can be done using three buses type: voltage controlled bus (PV), load bus (PQ) and droop-controlled bus (DB). Nevertheless, none of these bus types can represent the droop-controlled DG units with secondary control for frequency and voltage restoration. In this regard, this section presents the procedure for the incorporation of the hierarchically controlled DG units for islanded AC microgrids in the well-known power flow method [45].

2.5.2.1 Active power droop control and frequency restoration formulation

The active power output of each DG unit is governed by equation (1.9), which in turn depends on the frequency restoration output of the secondary control. According to (1.9), with $\omega_m = \omega^*$, where the subscript m indicates the bus controlled by the secondary control, the active power reference of the n-th DG unit becomes,

$$P_n^{ref} = \frac{u_\omega^{int}}{K_n^p} \tag{2.34}$$

where u_ω^{int} is the output of the frequency secondary control integrator $\left(k^{iw}\int(\omega^* - \omega_m)dt\right)$ in steady-state and it is calculated as shown below.

The bus phase angle θ_m, where the secondary control measures the frequency, is related with the angle δ_m in the following way,

$$\theta_m = \omega^* t + \delta_m \tag{2.35}$$

where t is the time. Observe that if (2.35) is derived with respect to the time, the following expression results,

$$\frac{d\delta_m}{dt} = \omega_m - \omega^* \tag{2.36}$$

Thus, (2.36) can be substituted in the integral part of (1.7); then by integrating u_ω^{int}, the following expression is obtained,

$$u_\omega^{int} = -k^{iw}(\delta_m - \delta_m^0) \tag{2.37}$$

where δ_m^0 is an initial condition. Note that, if the phase reference is shifted due to the SRF-PLL measurements as mentioned in Section II, the change is reflected in δ_m^0. In this work the SRF-PLL measures the q voltage component (v_q), therefore, the output will be shifted 90 degrees.

Merging (2.34) and (2.37), it is observed that P_n^{ref} depends on the bus angle (δ_m) where the bus is being controlled by the secondary control, the integration gain (k^{iw}), the droop gain (K_n^P), and the initial constant value,

$$P_n^{ref} = \frac{-k^{iw}(\delta_m - \delta_m^0)}{K_n^p} \tag{2.38}$$

Therefore, using (2.38) and scaling it to p.u. using S_{base}, the equation that has to be solved for the active power ΔP_n is as follows,

$$\Delta P_n = P_n - P_n^{ref} = P_n - \frac{-k^{iw}(\delta_m - \delta_m^0)}{K_n^p}\frac{1}{S_{base}} \tag{2.39}$$

Note that in (2.39) only appears the control gains that modify the steady-state solution. Furthermore, it is shown that the secondary control sets the reference phase angle for all the DG units. This finding shows that regarding power flow formulation, the slack bus is not needed, but instead, all the DG units share the injected power. Consequently, the use of an adaptive slack bus [46] or the fixing of a bus phase angle to zero [4] are avoided.

2.5.2.2 Reactive power droop control and voltage amplitude restoration formulation

According to (1.10), the power flow model for the reactive power of the n-th DG unit, can be written as follows,

$$Q_n^{ref} = \frac{|V_n^*| - |V_n| + u_v^{int}}{K_n^q} \tag{2.40}$$

where u_v^{int} is the integrator output of the secondary voltage control in steady-state. In this case, there is no equation related to the integral part of the secondary voltage control such as in the secondary frequency part; however, it is known that in steady-state, the voltage at the controlled bus is going to be fixed to the value of the secondary voltage control reference ($|V_m| = |V^{**}|$), therefore, the reactive power equation related to the controlled bus is used to compute the value of u_v^{int}. In this way, there is no change in the formulation due to the secondary voltage control and the reactive power formulation ΔQ_n is as follows,

$$\Delta Q_n \;=\; Q_n - \frac{|V_n^*| - |V_n| + u_v^{int}}{K_n^q}\frac{V_{base}}{S_{base}} \tag{2.41}$$

Finally, the mismatching equations of the new controlled bus needed by the power flow formulation, which will be called as hierarchically controlled PQ (HCPQ) bus from now, can be summarized as follows,

$$\begin{bmatrix} \Delta P_n \\ \Delta Q_n \end{bmatrix} = \begin{bmatrix} P_n - \dfrac{-k^{iw}(\delta_m - \delta_m^0)}{K_n^p}\dfrac{1}{S_{base}} \\ Q_n - \dfrac{|V_n^*| - |V_n| + u_v^{int}}{K_n^q}\dfrac{V_{base}}{S_{base}} \end{bmatrix} \tag{2.42}$$

Now, each hierarchically controlled DG unit can be included in the power flow model in the form of the new HCPQ bus, this is schematically shown in Fig. 2.9.

According to (2.40), the controlled reactive power is based on the measured capacitor voltage shown in Fig. 2.9, and this voltage is adjusted by the primary control; thus the LC filter is embedded in the HCPQ bus.

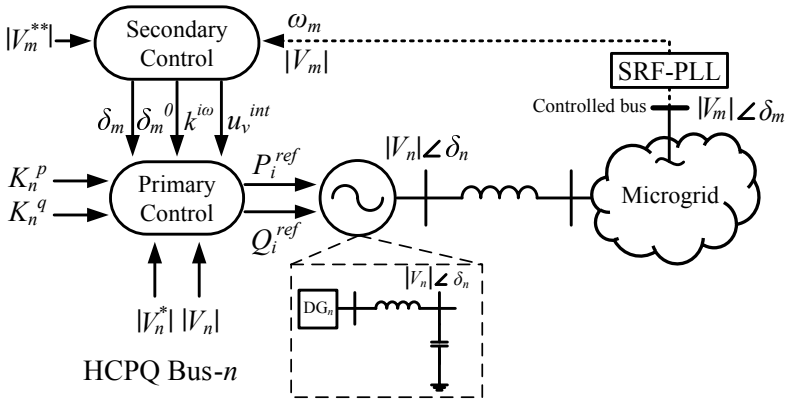

FIGURE 2.9: HCPQ bus diagram.

2.5.2.3 Reactive power droop control and voltage amplitude restoration: system reduction

Observe that, if the DG units are connected to the bus where the voltage is restored by the secondary control, a reduction of the system can be made. For explanation, Fig. 2.10 shows the single-line diagram of a DG unit connected through a feeder to the PCC where the secondary control restores the voltage.

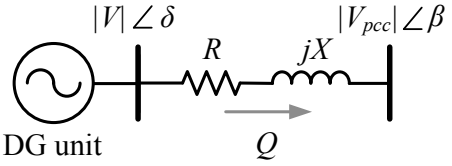

FIGURE 2.10: Single-line diagram of a DG unit connected to the PCC bus.

From Fig. 2.10, the reactive power flowing from the DG unit to the PCC, can be computed as,

$$Q = -\left(|V|^2|Y|sin(\theta) - |V||V_{pcc}||Y|sin(-\delta+\beta+\gamma)\right) \tag{2.43}$$

where $|V_{pcc}|$ is known since it is a controlled voltage ($|V_{pcc}| = |V^{**}|$), β is the phase angle of $|V_{pcc}|$, as seen in Fig. 2.10, and γ is the admittance angle. Merging (2.40) and (2.43) yields to,

$$|V|^2|Y|sin(\gamma) - |V||V_{pcc}||Y|sin(-\delta+\beta+\gamma) + \frac{|V^*| - |V| + u_v^{int}}{K^q}\frac{V_{base}}{S_{base}} = 0 \tag{2.44}$$

this equation can be rearranged as,

$$|V|^2|Y|sin(\gamma) + |V|(-|V_{pcc}||Y|sin(-\delta+\beta+\gamma) - \frac{1}{K^q}\frac{V_{base}}{S_{base}}) + \frac{|V^*| + u_v^{int}}{K^q}\frac{V_{base}}{S_{base}} = 0 \tag{2.45}$$

Computing the roots of (2.45), the voltage $|V|$ can be obtained. In this way, since the voltage of the new controlled bus HCPQ is already known, the mismatching equations needed in the power flow formulation are reduced as follows,

$$\Delta P_n = P_n - \frac{-k^{iw}(\delta_m - \delta_m^0)}{K_n^p}\frac{1}{S_{base}} \tag{2.46}$$

Finally, combining the model of HCPQ from equation (2.42), and the PV and PQ buses from the conventional power flow method, the power flow formulation of the whole system can be summarized as follows,

$$\left.\begin{aligned} P_n - \frac{-k^{iw}(\delta_m - \delta_m^0)}{K_n^p}\frac{1}{S_{base}} &= 0 \\ Q_n - \frac{|V_n^*| - |V_n| + u_v^{aux}}{K_n^q}\frac{V_{base}}{S_{base}} &= 0 \end{aligned}\right\} \text{HCPQ bus}$$

$$\left.\begin{aligned} P_n - P_n^{sch} &= 0 \\ Q_n - Q_n^{sch} &= 0 \end{aligned}\right\} \text{PQ bus} \tag{2.47}$$

$$\left.P_n - P_n^{sch} = 0\right\} \text{PV bus}$$

where P_n and Q_n are the injected active and reactive powers [37], and they are expressed as shown in (2.28) and (2.29), respectively. Note that the HCPQ bus can be replaced by (2.46) if the DG units are connected to the bus controlled by the secondary voltage control.

2.6 Power flow model evaluation

This section presents two evaluation cases of the proposed power flow model for hierarchically controlled islanded microgrids. In the first case, a comparison among the obtained steady-state solutions with the proposed models, and the steady-state solutions obtained with the complete time-domain models using two professional simulators, PSCAD and MATLAB/Simulink, is performed. Additionally, an analysis of the convergence behavior for different X/R transmission line ratios in resistive microgrids is presented.

In order to show the difference among the solutions obtained with the hierarchically-controlled MG and the droop-controlled MG, the second case study presents the differences between the power flow solutions obtained with the hierarchical control (HCPQ bus) and with the primary control (DB bus) against the variation of Load 4 (shown in the case study system). The Load 4 is varied as follows,

$$P_{L,4} = P^0_{L,4}(1+\lambda) \tag{2.48}$$

$$Q_{L,4} = \sqrt{\frac{P^2_{L,4}}{PF^2_{L,4}} - P^2_{L,4}} \tag{2.49}$$

where λ is the loading factor, and PF is the power factor of the load. Additionally, in this case the secondary voltage control reference is $|V^{**}| = 1$ for all the DG units, and the nominal bus 4 load is $P^0_{L,4} = 15$ kW with a lagging power factor of 0.89.

The power flow equations are solved using the Newton-Raphson method. The MATLAB/Simulink simulations are conducted using the fundamental frequency model, using the *ode15s* integration method with absolute and relative tolerances of 1×10^{-6}. On the other hand, PSCAD enables the switching process of the power electronic interface of the DG units, using an integration time step of 0.05×10^{-6}. The studies were performed in a MacBook Pro with a processor of 2.5 GHz Intel Core i5 and 16 GB of RAM. A convergence error tolerance of 1×10^{-8} was used.

2.6.1 Case study system

Figure 2.11 shows the single-line diagram of the test system. The microgrid includes 5 DG units and an AC voltage source. The DG units and AC voltage source interact

with each other through RL lines and share the AC common bus where the secondary frequency control acts; the secondary voltage control acts at the different PCCs [19]. The microgrid contains linear loads and a voltage-dependent non-linear load connected to the AC common bus. The HCPQ buses represent the DG units, the PQ buses represent the loads, and the PV bus represent the AC voltage source. Table 2.5 shows the parameters of LC filters, feeders, and primary controls. The case study considers the same PI control gains for all the DG units; however, the droop characteristics are different for the DG units as shown in Fig. 2.11. Additionally, the line impedances and the voltage references for the restoration control ($|V^{**}|$), are also shown in Fig. 2.11; the parameters of the line impedances were extracted from [25]. The proportional and integral gains were calculated based on stability constrains. This was performed based on a small-signal analysis previously proposed, and interested readers may refer to [47] in which a small-signal stability analysis is performed for an islanded microgrid.

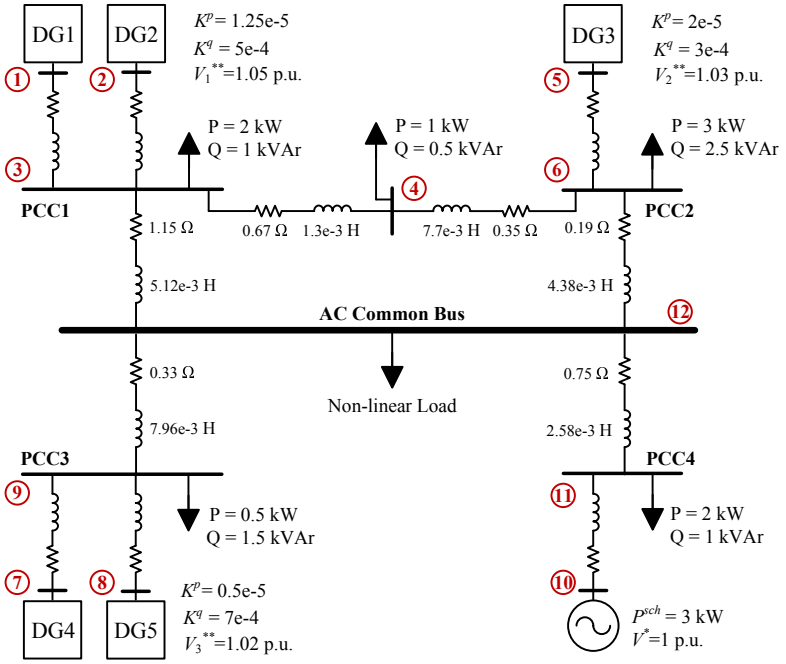

FIGURE 2.11: Single-line diagram of the second case study microgrid.

The nonlinear industrial load at bus 12 expressed as [48],

$$P_{L,12} = P^0_{L,12} V^{\alpha}_{12} \tag{2.50}$$

$$Q_{L,12} = Q^0_{L,12} V^{\beta}_{12} \tag{2.51}$$

TABLE 2.5: Parameters of the case study microgrid and control

Parameter	Symbol	Value
Nominal voltage	V_{L-L}^{RMS}	400 V
Nominal frequency	f^*	50 Hz
Nominal DC voltage	V_{DC}	1500 V
Filter resistance	R_{11}, R_{12}, R_{21}, R_{22}, R_{31}, R_{32}	0.1 Ω
Filter inductance	L_{11}, L_{21}, L_{31},	1.8 mH
Filter capacitance	C_{11}, C_{21}, C_{31}	27 μF
Feeder resistance	R_{13}, R_{23}, R_{33}	0.1 Ω
Feeder inductance	L_{12}, L_{22}, L_{32}	1.25 mH
Current loop proportional gain	k_{pc}	20
Current loop integral gain	k_{ic}	40
Voltage loop proportional gain	k_{pvo}	2.4×10^{-2}
Voltage loop integral gain	k_{ivo}	4.5
Frec. rest. proportional gain	k^{pw}	0.02
Frec. rest. integral gain	k^{iw}	4
Voltage rest. proportional gain	k^{pv}	0.2
Voltage rest. integral gain	k^{iv}	4
Switching frequency	f_c	10 kHz

where $\alpha = 0.18$, $\beta = 6$, $P_{L,12}^0 = 0.5$ p.u., $Q_{L,12}^0 = 0.3$ p.u., and $S_{base} = 10$ kVA.

2.6.2 Case study I: meshed multi-bus microgrid

Table 2.6 shows steady-state voltage magnitudes and phase angles given by the power flow solution, MATLAB/Simulink, and PSCAD. Observe that in the worst case, the proposed power flow gives errors of 5.112×10^{-6} and 1.581×10^{-3} as compared to MATLAB/Simulink and PSCAD, respectively. The errors are due to the different modeling approaches, the time steps, and the integration methods. In the case of PSCAD, the additional active and reactive power losses owing to the harmonic distortion generated by the power electronics inverters of each VSC increase the differences.

Figure 2.12 shows the active and reactive powers injected by the DG units, computed with the power flow method, MATLAB/Simulink, and PSCAD. The obtained results corroborate the effectiveness of the proposed power flow modeling to represent the hierarchical control of the MG.

TABLE 2.6: Case Study I: Computed Voltages with the Proposed Power Flow Method, Simulink and PSCAD

Bus	Power Flow (PF)	Simulink (averaged model)	PSCAD (switched model)	Error of PF vs. Simulink	Error of PF vs. PSCAD
1	1.0585268 $\angle 88.176199^o$	1.0585276 $\angle 88.176313^o$	1.0569459 $\angle 88.173563^o$	2.252×10^{-6}	1.581×10^{-3}
2	1.0585268 $\angle 88.176199^o$	1.0585276 $\angle 88.176313^o$	1.0569459 $\angle 88.173563^o$	2.252×10^{-6}	1.581×10^{-3}
3	1.05 $\angle 88.103490^o$	1.0499999 $\angle 88.103605^o$	1.0484303 $\angle 88.099824^o$	2.109×10^{-6}	1.571×10^{-3}
4	1.0430266 $\angle 88.297780^o$	1.0430265 $\angle 88.297838^o$	1.0414725 $\angle 88.295259^o$	1.060×10^{-6}	1.554×10^{-3}
5	1.0405431 $\angle 88.483247^o$	1.0405448 $\angle 88.483304^o$	1.0390094 $\angle 88.486513^o$	1.990×10^{-6}	1.534×10^{-3}
6	1.03 $\angle 88.508686^o$	1.0300001 $\angle 88.508744^o$	1.0284684 $\angle 88.510806^o$	1.047×10^{-6}	1.532×10^{-3}
7	1.0240570 $\angle 95.913364^o$	1.0240571 $\angle 95.913650^o$	1.0224847 $\angle 95.918692^o$	5.112×10^{-6}	1.575×10^{-3}
8	1.0240570 $\angle 95.913364^o$	1.0240571 $\angle 95.913650^o$	1.0224847 $\angle 95.918692^o$	5.112×10^{-6}	1.575×10^{-3}
9	1.02 $\angle 95.463305^o$	1.0199999 $\angle 95.463592^o$	1.0184334 $\angle 95.467373^o$	5.110×10^{-6}	1.568×10^{-3}
10	1 $\angle 91.212589^o$	0.9999999 $\angle 91.212646^o$	0.9984393 $\angle 91.212646^o$	9.998×10^{-7}	1.560×10^{-3}
11	1.0021472 $\angle 90.733596^o$	1.0021462 $\angle 90.733539^o$	1.0005936 $\angle 90.733768^o$	1.412×10^{-6}	1.553×10^{-3}
12	1.0110652 $\angle 89.745931^o$	1.0110633 $\angle 89.745989^o$	1.0095279 $\angle 89.746447^o$	2.158×10^{-6}	1.537×10^{-3}

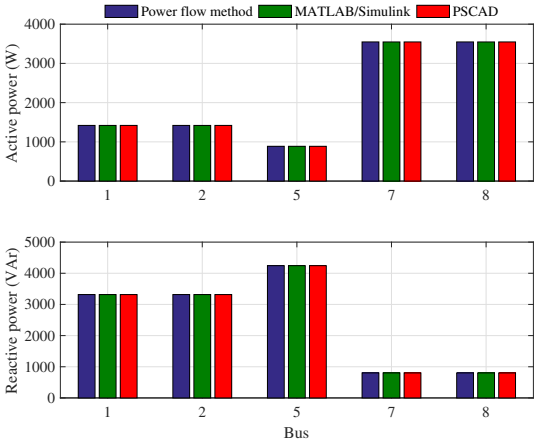

FIGURE 2.12: Comparison of the active and reactive powers injected by the DG units given by the power flow method, MATLAB/Simulink and PSCAD in Case I.

The salient features of the power flow are the computational speed and convergence rate, in this regard, Table 2.7 shows the convergence mismatches on three different operation conditions: nominal condition shown in Fig. 2.11, all loads increased by 50%, and all loads doubled. Notice that the method has a quadratic convergence characteristic even with load increments and achieves the solution, in all cases, in only four iterations and 0.145 seconds. Table 2.7 also shows that the Newton-Raphson-based power flow reduces its convergence rate as the load increases as expected [27].

TABLE 2.7: Convergence errors of the Case I

Iteration	Power Flow, Nominal P & Q loads	Power Flow, P & Q loads increased by 50%	Power Flow, P & Q loads increased by 100%
1	1.644×10^{-2}	2.355×10^{-2}	3.061×10^{-2}
2	1.449×10^{-3}	1.410×10^{-3}	1.450×10^{-3}
3	4.813×10^{-6}	6.830×10^{-6}	1.068×10^{-5}
4	8.519×10^{-11}	1.591×10^{-10}	4.207×10^{-10}

As is shown in this case studies, the power flow method has a good performance regarding the execution time and convergence rate. Furthermore, the steady-state solution obtained with the proposed power flow model is as good as the one obtained with the professional time-domain simulation programs. To evaluate the convergence characteristic of the proposed power flow in a dominantly resistive MG, the transmission lines parameters of the microgrid of Fig. 2.11 were changed to reduce their X/R ratio 16 times. Line inductances were reduced four times, and line resistances were increased four times. Under this condition, the Newton-Raphson method converges in 6 iterations with an error of 2.2297×10^{-13}, but still preserves its quadratic convergence feature.

Additionally, it is worth mentioning that due to the numerical method used to solve the power flow problem is the Newton-Raphson, the microgrid can be meshed, radial, dominantly resistive or inductive [45].

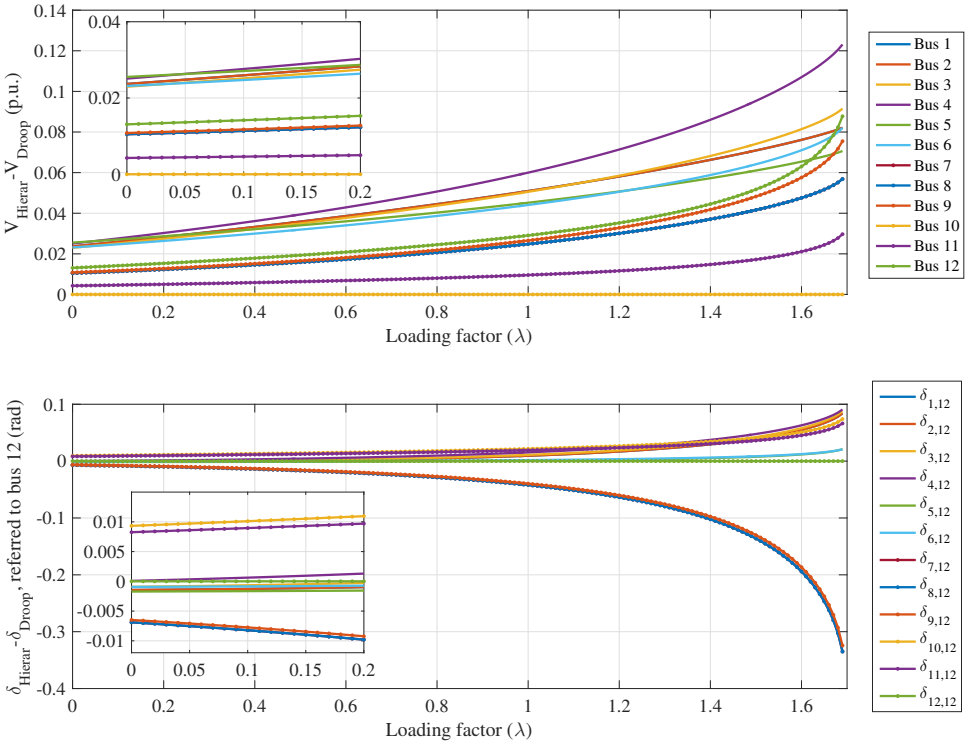

FIGURE 2.13: Differences of the steady-state buses voltage magnitudes and phase angles, solving the system with the power flow method using the HCPQ bus and the droop bus, for the bus 4 load variation.

2.6.3 Case study II: Power flow comparison, HCPQ bus against droop bus

Figure 2.13 shows the differences between the bus voltages obtained with the proposed HCPQ bus and the droop bus, versus load changes. Notice that the voltage magnitude differences ($V_{Hierar} - V_{Droop}$) are positive since the voltage drop with the droop-based control is larger in all buses, except bus 10 because it is a PV bus. This behavior is expected since the droop-based control does not restore the voltage deviations. Furthermore, the voltage drops with the droop-based control increase the currents, which provoke an increment of losses as compared with the hierarchical control.

On the other hand, the phase angles differences show positive and negative evolutions, which also increase as the load increases. As mentioned before, the reference angle is

imposed by the secondary control, therefore, as shown in Fig. 2.13, the phase angles achieved by the hierarchically controlled MG case are different to those obtained with the droop- based controlled MG case, in which case, a phase angle has to be fixed.

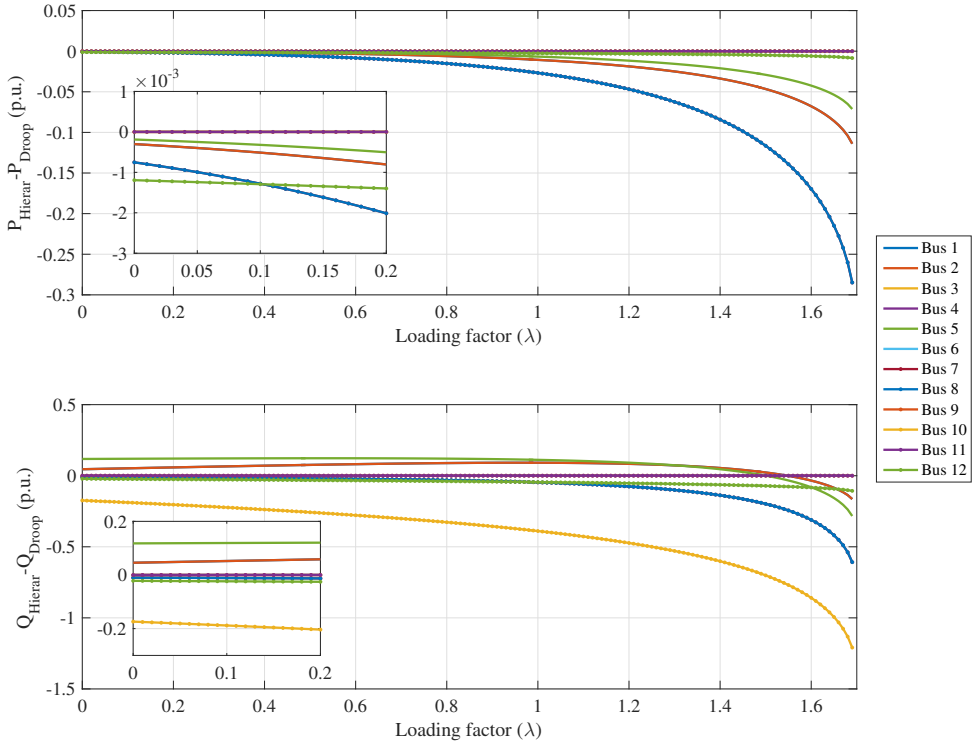

FIGURE 2.14: Differences of the steady-state active and reactive power, solving the system with the power flow method using the HCPQ bus and the droop bus, versus load 4 variation.

Figure 2.14 shows the differences between the powers injected by the hierarchically controlled MG and the droop-based controlled MG under variation of the load at bus 4. Observe that for light loads, the injected active powers by both control schemes are close each other; however, for larger loads, the differences increase, except for bus 10 because it is a PV bus. Note that the differences increase considerably for large loads, being the droop-based approach the one that has more significant active power injections. Please notice that in the droop control case, the DG units inject more reactive power than in the hierarchically controlled case. This behavior is owing to the lack of voltage regulation, which also causes more power losses.

The differences shown in this case study, exhibit the importance of using hierarchically controlled power flow models when the DG units include secondary controls for voltage and frequency restoration. Power flow based analyses are widely used in industry. Therefore, accurate modeling is essential to achieve reliable steady-state solutions. It

is demonstrated that the proposed HCPQ bus enhances the reliability of power flow solution of hierarchically controlled islanded microgrids.

2.7 Discussions

This chapter presented different methods for the computation of the steady-state solution of AC microgrids, i.e., Newton methods, Newton methods including parallel cloud computing, droop-based extended power flow and the hierarchical extended power flow. Furthermore, for each method a detailed explanation of its formulation was presented and case studies for the model and performance evaluations were addressed.

The results obtained showed the advantages and drawback of each method. The Newton methods can capture the harmonic information and tell us about the stability of the system; however, the CPU time required is large. On the other hand, the power flow formulations require small CPU times, but only fundamental frequency can be taken into account. Thus, depending on the analysis or application required, both methods can be useful and reliable.

In this way, the application of the methods for the steady-state computation and control of AC microgrids is performed in the next chapters.

Chapter 3

Hierarchical control of islanded AC microgrids

The increasing integration of DG units has meant a modernization of the current electric power system by providing more reliability and sustainability [4–6]. However, due to the distributed operation of the generation units, new technical challenges have emerged mainly related to the voltage quality along the feeders and the proper power sharing considering the capacity and characteristics of the DG units [49, 50].

As a matter of fact, islanded microgrids represent an additional challenge since the DG units should perform a multifunctional operation. Apart from supplying power and ensuring the local demand, they should participate actively in the regulation of the islanded power system [51]. Several authors have addressed these challenges by developing different variants of primary controllers for achieving the power-sharing function among DG units [11]. Particularly, the droop-based methods have been widely used in the literature due to their characteristics and advantages, such as high flexibility, reliability, and capability of managing active and reactive power sharing by relying only on local measurements without the use of additional communication among DG units [1, 3].

Commonly, the DG units are interconnected through long radial feeders since they are usually far from the load location. However, due to the line impedance among DG units, serious problems appear related to power losses, reactive power flow and voltage quality along the feeders [50, 52, 53]. This kind of problems cannot be solved directly by the primary controllers, which require the support of complex control schemes for enhancing the operational characteristics required in the microgrids by providing power flow control and voltage regulation along the feeders [1, 11]. Hence, to cope with this problem, hierarchical controls have been proposed in the literature [11, 54–58].

In previous literature, different mathematical methods and hierarchical schemes for the power flow based optimized operation of islanded microgrids have been presented; however, offline schemes without experimental validation are presented. In this way, laboratory implementations are needed to validate that in practical environments, the proposed approaches have a close performance as in simulation stages even with system characteristics that were not modeled in the design stage.

Regarding the aforementioned, in this work a laboratory-scale evaluation of an optimal power flow as a hierarchical control for the online operation of islanded microgrids is presented. Additionally, in order to emulate practical situations encountered in islanded microgrids and to test the online optimization included in the hierarchical control, the case studies include random load profiles, random capacity profiles, efficiency curves for the conversion units, and the use of practical measurement instruments (smart meters) for the control action, showing the challenges, advantages and drawbacks of the proposed control scheme. Furthermore, in order to give a self-content work which can be able to be reproduced, this chapter presents a detailed description of the controls, parameters, the equipment and software used for the implementation. On the other hand, it is important to mention that, the optimization is made online and is activated when changes in the loads or the generation capacities occur, allowing an optimal operational performance for unpredicted loads or generation capacities changes in the islanded microgrid.

The proposed hierarchical control scheme includes a primary conventional droop control and a centralized extended optimal power flow (EOPF) control which is responsible of the active and reactive power sharing management. The online optimization is based, but not limited, on three operational objectives, i.e., efficiency improvement, voltage regulation and generation capacity constrains for the DG units. It is important to notice that, unlike the control schemes which incorporate the power flow for power sharing [1], in the proposed hierarchical scheme, the control dynamics of each DG unit are taken into account by including the droop characteristics in the conventional power flow formulation. In this way, the optimization of the droop characteristic coefficients and voltage references of the primary DG unit controls can be performed in order to achieve the operational objectives. Furthermore, since the control scheme is based on the extended optimal power flow, it is not limited to a specific islanded microgrid topology, therefore, it can be easily modified in the EOPF control stage.

3.1 EOPF hierarchical control

As presented in Chapter 1, the level of contribution of each DG unit in the power balance of the islanded system depends on the frequency/active power (P-ω) and voltage/reactive power (Q-V) droop characteristics. In accordance to the active and reactive power demand, the droop characteristics will determine the resultant angular frequency of the islanded power system (ω) and the voltage (V_n) of each DG unit. In this sense, it is possible to define the steady-state operation of each DG by adjusting the parameters of the droop characteristics.

Commonly, the DG units are integrated through feeders since the energy sources may be located away from the load centers and points of common coupling (PCCs) as shown in Fig. 3.1 [59]. In this way, the reactive power sharing is affected by the line impedance along feeders [60, 61], additionally, the voltage quality at the PCCs and load centers may be compromised due to the effect of the (Q-V) droop control loops, and the voltage drop across the line impedance. On the other hand, the (P-ω) droop control can achieve an accurate active power sharing [62]; however, the total power contribution of each DG may be determined by the rated power of each energy resource.

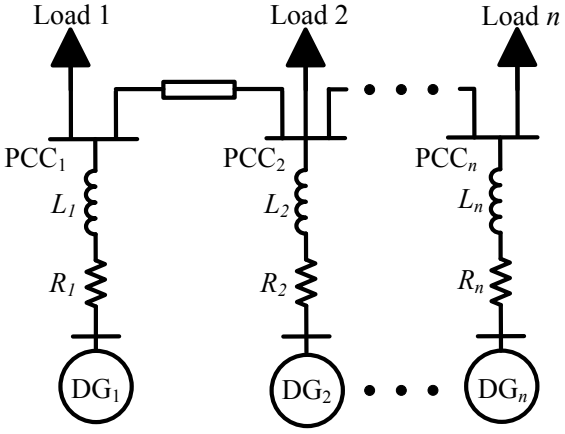

FIGURE 3.1: Single line diagram of a microgrid with multiple feeders.

On top of that, heterogeneous energy resources may require conversion stages of different characteristics in order to enable the integration of the primary energy resource to the power AC grid. This fact means different efficiencies in the conversion process, which should be also considered for defining the power contribution of each DG in order to enhance the global efficiency of the islanded microgrid [63].

Regarding the aforementioned, the proposed EOPF hierarchical control has the purpose of managing the active and reactive power sharing, to achieve the specific operational goals of the islanded microgrid, such as:

- Maximize the global efficiency of the microgrid.
- PCC voltage regulation.
- Maintain the active and reactive power supplied by the DG units within its capacities.

These goals are reached through the optimal selection of the droop characteristic coefficients K_n^p and K_n^q, and voltage references of each DG unit in accordance to (1.1) and (1.2), which are included in an extended power flow formulation.

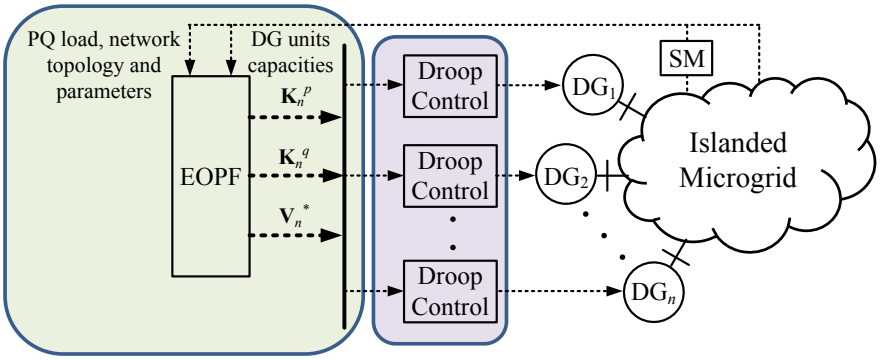

FIGURE 3.2: Hierarchical control scheme.

The proposed hierarchical control includes a primary conventional droop control and a centralized extended optimal power flow control level. The EOPF control level is responsible of computing and sending the droop references K_n^p, K_n^q, and V_n^* for each DG unit primary control as shown in Fig. 3.2. In order to perform this computation, the information of the microgrid topology, loads and DG units capacities are needed, additionally, a set of constrained nonlinear functions representing the operational goals is required by the optimization method.

It is important to mention that, the online operation of the EOPF control is activated when changes in the load or in the DG units capacities occur, in this way, this is an important contribution compared to conventional approaches based on offline optimization schemes. In this work, the changes of generation capacities are performed by random profiles for each DG unit to emulate the changes in the primary energy resources, i.e., wind, solar, among others; however, commonly the capacity information is sent from a tertiary control, such as, energy management systems (EMS) [64].

In light of the above, a detailed explanation of each stage of the hierarchical control scheme, i.e., primary control, extended power flow and the optimization formulation are addressed below.

3.1.1 Hierarchical control scheme

The hierarchical control includes a primary droop control, which is responsible for performing the grid-forming function, and a second control layer for the optimal operation of the MG. The voltage and frequency references for the voltage sources are derived from the droop control loops, which in turn, receive the droop coefficient (K_n^p, K_n^q) and voltage reference (V_n^*) values from the centralized EOPF control as shown in Fig. 3.3.

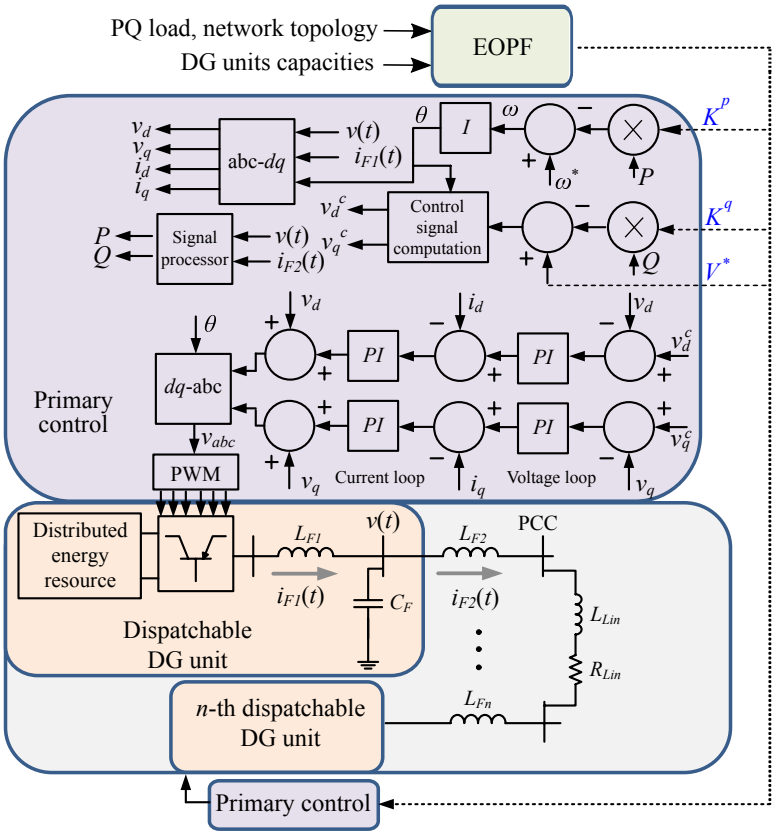

FIGURE 3.3: Control block diagram of the hierarchical scheme.

Due to changing operating circumstances (i.e., the profiles of generation from the DGs and consumption from the loads) the parameters of the droop characteristics, which are defined by the centralized EOPF, should be adjusted for achieving the operational goals of the islanded microgrid. The variations in the parameters of the droop characteristics, and more specifically in the droop coefficients (K_n^p and K_n^q) affect directly the dynamic and steady-state performance of the islanded power system (K_n^p and K_n^q). Because of that, it is important to define the nominal values for the droop coefficient that ensure the stability and proper dynamic behavior of the microgrid. It is worth mentioning that the proportional-integral controllers gains were obtained based on a bode analysis of the transfer function of the system, but other techniques can be used.

3.1.2 Extended optimal power flow formulation

From Chapter 2, is shown that the control references K_n^p, K_n^q, and V_n^*, which affect the steady-state behavior of the islanded microgrid, appear explicitly in the power-flow DB bus formulation. Consequently, an optimal power flow can be formulated by using the DB bus as a base, as shown in the next section.

3.1.2.1 Optimization problem formulation

In order to compute the droop characteristics and voltage reference of each DG unit, an optimization problem has to be solved. The formulation of the problem is specified as follows,

$$min_x\ f(\mathbf{x})\ such\ that \begin{cases} c(\mathbf{x}) \leq 0 \\ lb < \mathbf{x} < ub \end{cases} \tag{3.1}$$

where $\mathbf{x}$ are the variables to optimize, $f(\mathbf{x})$ is the function to minimize, $c(\mathbf{x})$ is a non-linear function, and lb and ub the lower and upper bound restrictions for the $\mathbf{x}$ values, respectively.

The equations proposed for the optimization formulation are based on three operational goals of the islanded microgrid:

1. The losses of each DG unit is minimized based on their efficiency curves, maximizing the global efficiency of the microgrid.
2. The voltages on the PCCs are maintained close to 1 p.u. through reactive power management.
3. The power injected by the DG units cannot exceed its maximum capacity ($S_n < S_n^{max}$).

The variables to optimize are the droop characteristics and reference values of the primary control K_n^p, K_n^q, and V_n^*. The formulation of each operational goal as a function is explained in detail below.

DG units efficiency function. The efficiency of the DG units is defined based on the relationship between the output power delivered to the microgrid and the input power provided by the primary source [63],

$$\eta_n = \frac{P_n^{out}}{P_n^{in}} \tag{3.2}$$

this efficiency represents the losses due to conversion, switching of electronic devices, among others. Additionally, the total losses depend on the characteristics of the technology used, the operating point and the switching frequency [63].

In this way, the efficiency of an inverter can be represented graphically for all the load range that it is able to handle. These efficiency curves can be obtained with simulation or experimentally and approximated by a second order function as follows [63],

$$\eta_n = \frac{\alpha_n^1 P_n^{in} + \alpha_n^0}{P_n^{in^2} + \beta_n^1 P_n^{in} + \beta_n^0} \tag{3.3}$$

where α_n^1, α_n^0, β_n^1 and β_n^0 are the coefficients obtained with the simulation or experimental results of the n-th DG unit.

Hence, in a microgrid composed by n DG units, the global efficiency can be maximized with the reduction of the total losses in the DG units, taking into account that, in the test islanded microgrid the losses in the feeders can be neglected, otherwise, the conductor losses have to be taken into account.

Notice that (3.3) computes the efficiency using the P_n^{in} but in the power flow method the power computed is P_n^{out}, therefore, substituting $P_n^{in} = P_n^{out}/\eta_n$, (3.3) is reformulated and the following quadratic equation is obtained,

$$\eta_n^2 + \eta_n\Big(\frac{\beta_n^1}{\beta_n^0}P_n^{out} - \frac{\alpha_n^0}{\beta_n^0}\Big) + \frac{P_n^{out^2}}{\beta_n^0} - \frac{\alpha_n^1}{\beta_n^0}P_n^{out} = 0 \tag{3.4}$$

finally, solving (3.4) the value of η_n is obtained.

Regarding the aforementioned, this operational goal can be formulated in the optimization problem as follows,

$$\mathbf{F}_\eta = \sum_{n=1}^{N} (P_n^{in} - P_n^{out})^2 \tag{3.5}$$

where N is the number of DG units. Observe that, if all the DG units are working with an ideal efficiency ($\eta = 1$), the function F_η will be equal to zero, in this way, the minimization of this function will maximize the efficiency of the microgrid.

PCCs voltage regulation function. Since the power flow solution gives the system bus voltage magnitudes in p.u., the function used to achieve this operational goal can be formulated as follows,

$$\mathbf{F}_V = \sum_{n=1}^{N} (V_{PCCn} - V^{ref})^2 \tag{3.6}$$

notice that if the magnitudes of voltages V_{PCCn} are equal to the voltage reference $V^{ref} = 1$ p.u., the summation of the function will be equal to zero. It is important to note that the voltage in the different PCCs is related to the reactive power as shown in (1.2), in this way, the voltage is regulated with reactive power management (selecting K_n^q and V_n^*), without the need of an extra control loop.

Power restriction. The power restriction is included in the optimization problem as an inequality function in $c(\mathbf{x}) \leq 0$ as,

$$c(\mathbf{x}) = \mathbf{S}_n - \mathbf{S}_n^{max} \leq 0, \quad for\ n = 1, ..., N \tag{3.7}$$

while this inequality is true, the power injected by the n-th DG unit will not exceed its capacity.

Regarding the aforementioned, the optimization problem is built as a sum of each operational goal function, subject to the capacity restriction as follows,

$$\begin{aligned} min_x\ f(\mathbf{x}) &= \alpha \mathbf{F}_\eta + \beta \mathbf{F}_V \\ Subject\ to \quad \mathbf{S} - \mathbf{S}^{max} &\leq 0 \end{aligned} \tag{3.8}$$

where α and β are weights, the solution of this problem gives the control references $\mathbf{K}^p = [K_1^p, ..., K_n^p]$, $\mathbf{K}^q = [K_1^q, ..., K_n^q]$, and $\mathbf{V}^* = [V_1^*, ..., V_n^*]$. In order to have a better understating of the optimization, in Fig. 3.4 a flowchart of the EOPF is shown.

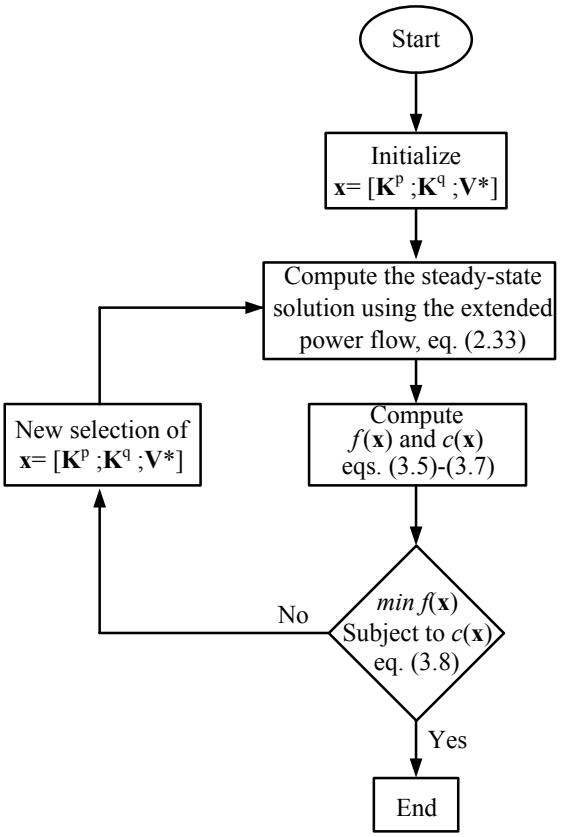

FIGURE 3.4: Control optimization flowchart.

Note that, since the optimal formulation is performed through the power flow, other operational goals can be added easily for different MG topologies that might need specific features, such as, losses minimization [65] (for both active and reactive power), cost minimization [66], among others.

It is important to mention that, in this work the problem is solved using the *fmincon* optimization tool of MATLAB, which for the test system used, has a good performance in terms of computation time, i.e., 1.58 seconds per optimization with an error tolerance of 1×10^{-6}; however, other optimization techniques can be used to solve the minimization problem shown in (3.8).

3.2 Test system and laboratory implementation

Figure 3.5 shows the single line diagram of the three-phase microgrid used as test system. It includes three dispatchable DG units with LC-filters connected to each PCC through

a RL feeder impedance, two fixed R loads wye-connected to PCC_1 and PCC_3, and a variable PQ load connected to PCC_2. Additionally, the PCCs are connected through RL lines and the variable load is measured by a smart meter (SM).

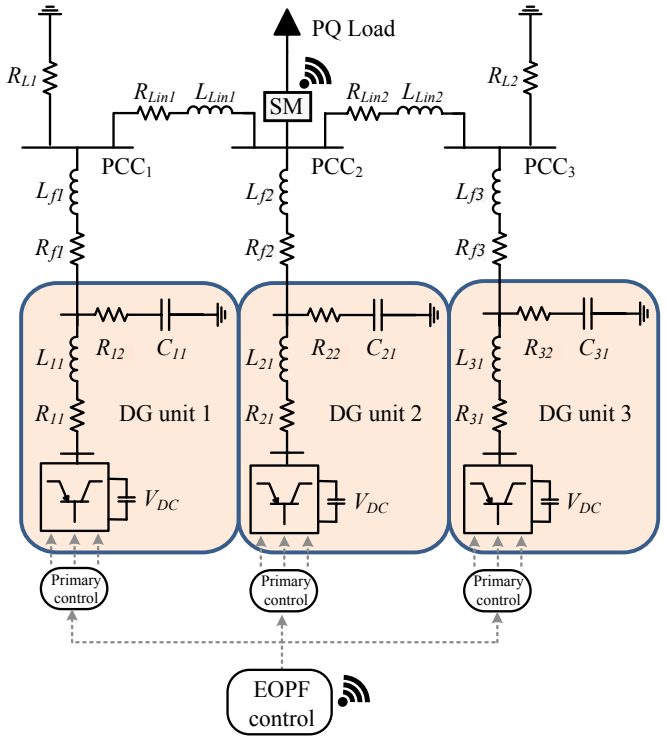

FIGURE 3.5: Single line diagram of the three-phase microgrid test system.

The primary control is modeled and included in a real time platform (dSPACE 1006), while the EOPF stage is incorporated in a central computer (CPC) which sends and receives information to the dSPACE via ethernet using a User Datagram Protocol (UDP) [67].

For the measurement of the variable load, a Kamstrup Smart Meter is used. The SM is connected to a central data base, which is responsible of handling and synchronizing the information sent by one or a cluster of SMs [68]. The communication implemented in the laboratory is the TCP/IP connection, which allows an easy incorporation of several SMs working over the same network structure [68].

The communication between the dSPACE and the CPC is performed through an interface using the professional software LabVIEW [69]. The SM is constantly sending the measures of the variable load to the central data base, which in turn sends the information to the CPC through the LabVIEW interface; if there is a change of load with respect to the last measurement received, it calls the MATLAB software to perform the optimization process. The CPC sends the computed control parameters to the dSPACE and it uses this information in the DG units primary control.

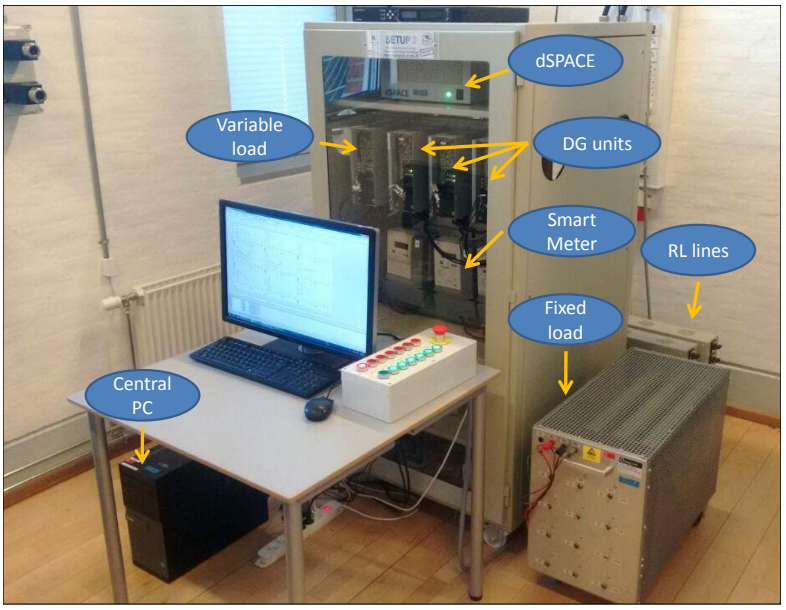

FIGURE 3.6: Laboratory implementation of the islanded microgrid.

The parameters of the test microgrid are shown in Table 3.1, they were obtained from the real values of the laboratory implementation, which was made in the Microgrid Research Laboratory in Aalborg University [67] with an online architecture as can be seen in Fig. 3.6.

TABLE 3.1: Parameters of the microgrid

Parameter	Symbol	Value
Nominal voltage	V_{L-L}^{RMS}	400 V
Nominal frequency	f^*	50 Hz
Nominal capacity	S^{max}	2.5 kVA
Nominal DC voltage	V_{DC}	650 V
Filter resistance	R_{11}, R_{12}, R_{21}, R_{22}, R_{31}, R_{32}	0.1 Ω
Filter inductance	L_{11}, L_{12}, L_{21}, L_{22}, L_{31}, L_{32}	1.25 mH
Filter capacitance	C_{11}, C_{21}, C_{31}	27 μF
Feeder resistance	R_{f1}, R_{f2}, R_{f3}	0.1 Ω
Feeder inductance	L_{f1}, L_{f2}, L_{f3}	1.25 mH
Line resistance	R_{Lin1}, R_{Lin2}	0.45 Ω
Line inductance	L_{Lin1}, L_{Lin2}	1.45 mH
Wye-resistance load	R_{L1}, R_{L2}	119 Ω

For the primary control level, Table 3.2 summarizes the nominal parameters selected for the case study microgrid. Please notice that, for all DG units in this work, for both PI

controllers in each loop (current and voltage) the parameters are the same.

TABLE 3.2: Parameters of the primary control

Parameter	Symbol	Value
$P-\omega$ droop coefficient	K^p	1.25×10^{-5}
$Q-V$ droop coefficient	K^q	1×10^{-3}
Current loop proportional gain	K_{pc}	20
Current loop integral gain	K_{ic}	40
Voltage loop proportional gain	K_{pv}	2.4×10^{-2}
Voltage loop integral gain	K_{iv}	4.5
Commutation frequency	f_c	10 kHz

Furthermore, the efficiency parameters used for the DG units were extracted from [63] and are shown in Table 3.3, additionally, the resulting efficiency curves of each DG unit is shown in Fig. 3.7.

TABLE 3.3: Parameters of the efficiency curves

Curve	α_n^1	α_n^0	β_n^1	β_n^0
η_1	7.317	-0.081	5.85	0.77
η_2	5.072	-0.037	4.4	0.18
η_3	8.249	-0.113	5.45	2.15

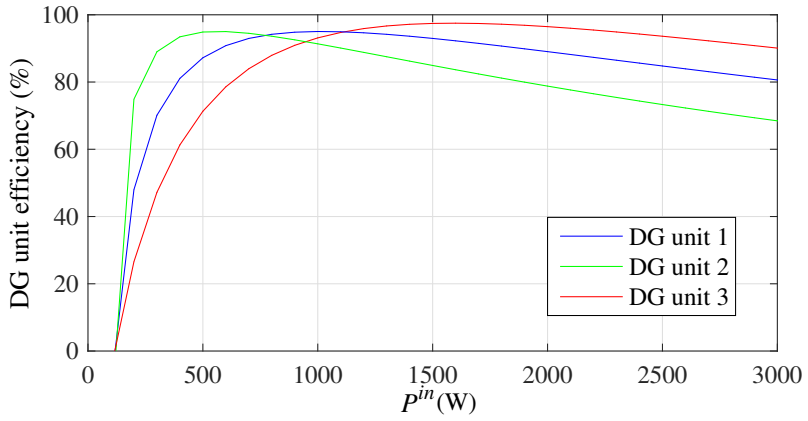

FIGURE 3.7: Efficiency curves of the DG units.

3.3 Case studies

To validate the proposed hierarchical scheme, in this section two case studies of the islanded MG under different practical operational conditions are presented. In the first case study, the load connected to the PCC_2 is changing following a load profile. The

load profile has 24 changes made every 30 seconds, emulating a load variation every hour in a day.

In a practical MG based on variable energy resources (solar, wind, etc.), the power that can be injected by the DG units is not always constant. In this way, power capacity profiles are included for each DG unit in the second case study, emulating the variation in the primary energy resources and to take into account this effect in the performance of the control.

In both cases, the control of the islanded microgrid is performed online using the hierarchical control and the measurements of the SM; however, in the first case study, the experiment is also conducted using only the conventional droop control to show the advantages of the proposed control scheme.

3.3.1 Case I: Load profile

The results obtained in this case for both, conventional droop control and the proposed hierarchical control, are shown in Fig. 3.8(a) and 3.8(b), respectively. Besides, the load profiles for active and reactive power and the capacities for the DG units are shown in Fig. 3.8(c).

Notice that, using the conventional droop control, due to the control references K_n^p, K_n^q, and V_n^* are the same for all the DG units, the active and reactive power shared among the units is very similar (Fig. 3.8(a.1) and 3.8(a.3)). Consequently, the efficiency of each DG unit is not taken into account in the operation of the microgrid as can be seen in Fig. 3.8(a.2), where in the worst case, drops up to 83 %. Additionally, observe that the PCCs voltage are always below 1 p.u., which in the worst case, drops up to 0.98 p.u. when the reactive power load is incremented.

On the other hand, using the EOPF control, observe in Fig. 3.8(b.1) that in order to get a better efficiency, each DG unit shares a different amount of active power depending on its efficiency curve. Notice Fig. 3.8(b.2) that, in the worst case, the efficiency drops up to 93 %. Additionally, in this case, the PCCs voltage are maintained close to 1 p.u., which in the worst case, drops up to 0.99 p.u.

Note that, the desired operational goals proposed are achieved taking into account random load variations and measurements from a practical Smart Meter. In this case, compared with the conventional droop control, the efficiency is improved 10 % and the voltage is regulated closer to the desired nominal value.

3.3.2 Case II: Load and capacity profiles

The results obtained for the second case study are shown in Fig. 3.9. The load and capacity profiles are shown in Figures 3.9(c) and 3.9(f), respectively. Notice that the capacity of the DG units changes constantly causing a variation of the active and reactive powers injected by the DG units, because of the restriction of the capacity limits included in the EOPF control.

Despite the changes of active and reactive power due to the capacity restriction, the PCCs voltage are kept close to the nominal voltage value, having in the worst case a drop up to 0.98 p.u. On the other hand, observe in Fig. 3.9(b) that the control tries to maximize the efficiency but the capacity restrictions limit the control optimization, i.e., if the n-th DG unit best efficiency is reached at 1.5 kW but the power capacity drops to 1 kW, it will not be able to reach its best efficiency.

The results obtained in the case studies show that the proposed hierarchical control is a reliable online scheme capable to manage different operational conditions, such as, random load and capacity profiles, and including practical devices such as the SM. On the other hand, the optimal extended power flow, which is based on the conventional formulation, has the advantage that any change in the microgrid topology can be updated in an easy and straightforward manner, besides, the operational goals can be also changed or improved depending on the operational needs of the islanded microgrid.

3.4 Discussions

The results obtained in the case studies revealed the applicability, advantages and drawbacks of the proposed hierarchical control scheme. It was shown that even with random PQ load and capacity variations, the proposed control, working online, regulates the voltage magnitude of the different PCCs and maximizes the efficiency of the DG units. On the other hand, notice that the computation time for the optimization method in the hierarchical control is less than 2 seconds which, in tertiary control schemes, is a good time for power management as seen in the results. Therefore, it is shown that the application of power flow based hierarchical control schemes contributes to the system to achieve optimized operating points in a reliable way.

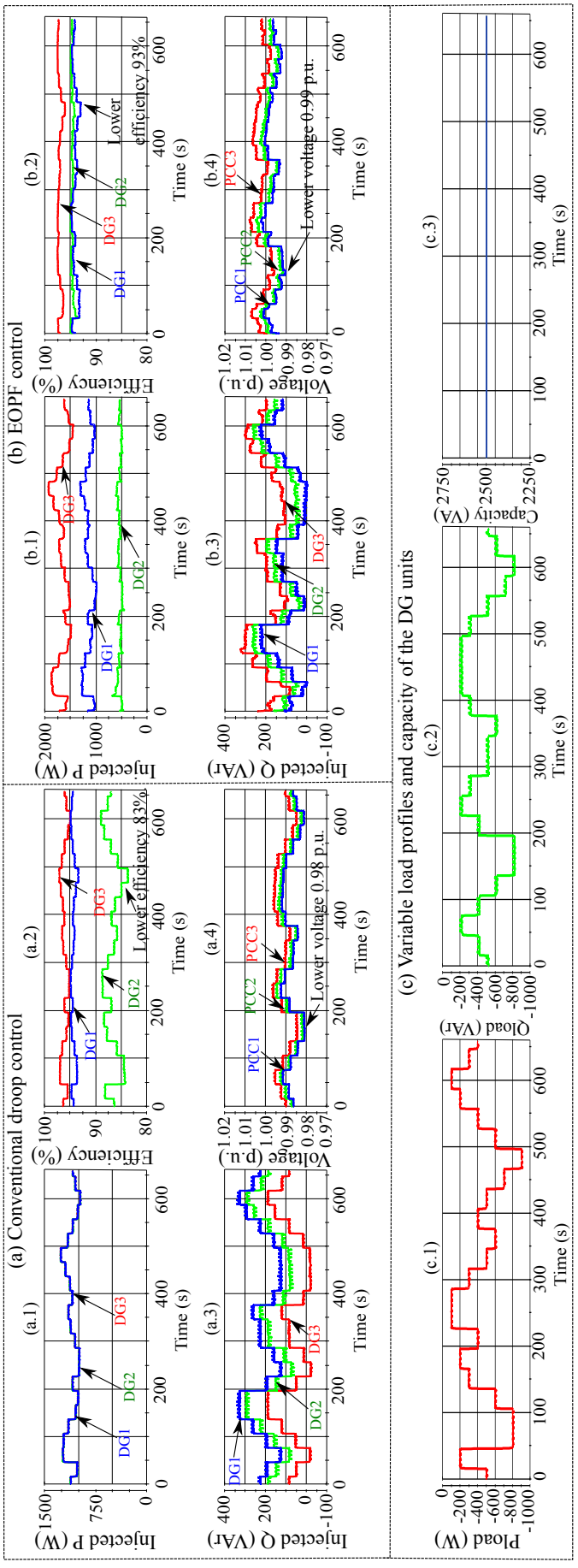

FIGURE 3.8: Case I: (a) conventional droop control response, (b) EOPF control response and (c) load and capacities profiles.

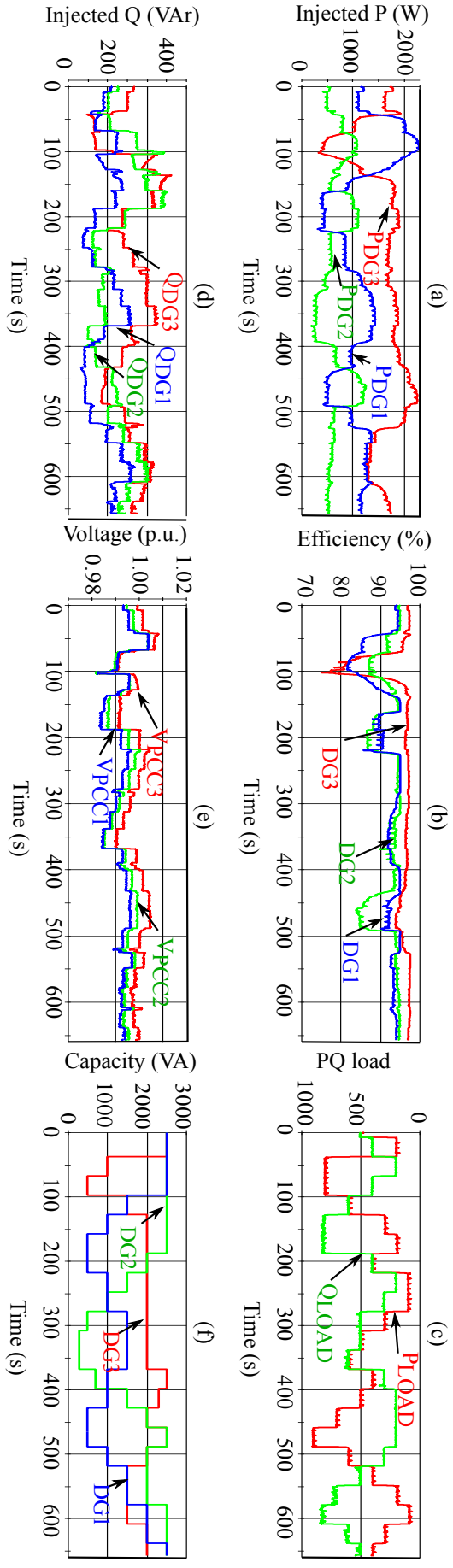

FIGURE 3.9: Case II: Hierarchical control scheme response under load and capacity profiles.

Chapter 4

Power-flow-based initialization of fast time-domain methods for the steady-state computation of nonsinusoidal AC microgrids.

As seen in Chapter 2, the computation of the steady-state solution of a controlled AC microgrid is not an easy task. Time and frequency domain approaches were addressed in the aforementioned chapter, and their advantages and drawbacks were highlighted. For time-domain approach, Newton methods were presented and they present quadratic convergence rate as well as they information about the stability of the system; however, the computation (CPU) time required can become a drawback for large and/or stiff systems. Likewise, for frequency-domain approach, power flow methods were presented, these methods require small CPU times and present quadratic convergence as well, however, the system can only be solved for the fundamental frequency, and the solution do not give information about the stability of the system.

To improve the steady-state computation, a methodology resembling a predictor-corrector method is presented in this chapter. The predictor-corrector methods are used for numerical continuation [27, 28], this is, given an initial point and a parameter variation, a prediction of the steady-state solution of a system is performed, this prediction is not completely accurate, so a correction is made. In this sense, a similar methodology can be applied to compute the steady-state solution of a controlled nonsinusoidal AC microgrid using the power flow and the Newton methods addressed in Chapter 2.

Firstly, a prediction of the microgrid steady-state solution is computed using the hierarchical extended power flow method. This solution includes only the fundamental frequency information, thus, a correction is needed to explicitly take into account the commutation process of the power converters. For the correction stage, the Newton methods are used. These methods use as initialization the power flow solution, and compute the steady-state solution including the harmonic information of the microgrid, therefore, the power flow solution is corrected by using the Newton methods.

This methodology which uses both Newton methods and power flow methods reduces the individual drawbacks before described, and maximizes their advantages, having a faster steady-state computation which includes the harmonic and stability information of the system. To test this methodology a case study is presented, where a comparison among the Newton methods using two initialization approaches is shown, i.e., the commonly n-full-cycles integration method, and the power flow method. The error mismatches of each Newton method and the CPU time required are presented.

4.1 Case study system

The test system single-line diagram is shown in Figure 4.1. The system includes 9 distributed generation units which are connected through RL feeders to different buses. The buses are interconnected by RL lines and share an AC common bus where the secondary frequency control acts. The secondary voltage control acts in buses 4, 9, 13 and 17. Table 4.1 shows the parameters of LC filters, feeders, and primary controls. The case study considers the same PI control gains for all the DG units; however, the droop characteristics are different for each DG unit as shown in Fig. 4.1. Additionally, the line impedances and the voltage references for the secondary control ($|V^{**}|$), are also shown in this figure. In time-domain approach, the system is modeled with 192 differential equations; but in frequency-domain approach, the HCPQ buses represent the DG units and the PQ buses the loads.

Figure 4.2 shows three full cycles of the DG unit 1 output currents in steady-state, it can be noticed that the MG steady-state solution is distorted due to the commutation process of the power electronic converters.

4.2 Steady-state computation assessment

In this section, the steady-state computation of the test system is performed using the Newton methods. The solutions obtained using an initialization of three full-cycles

TABLE 4.1: Parameters of the case study microgrid and hierarchical control

Parameter	Symbol	Value
Nominal voltage	V_{L-L}^{RMS}	400 V
Nominal frequency	f^*	50 Hz
Nominal DC voltage	V_{DC}	1500 V
Filter resistance	R	0.1 Ω
Filter inductance	L	1.8 mH
Filter capacitance	C	27 μF
Feeder resistance	R_f	0.1 Ω
Feeder inductance	L_f	1.25 mH
Current loop proportional gain	k_{pc}	20
Current loop integral gain	k_{ic}	40
Voltage loop proportional gain	k_{pvo}	2.4×10^{-2}
Voltage loop integral gain	k_{ivo}	4.5
Frec. rest. proportional gain	k^{pw}	0.02
Frec. rest. integral gain	k^{iw}	4
Voltage rest. proportional gain	k^{pv}	0.2
Voltage rest. integral gain	k^{iv}	4
Switching frequency	f_c	10 kHz

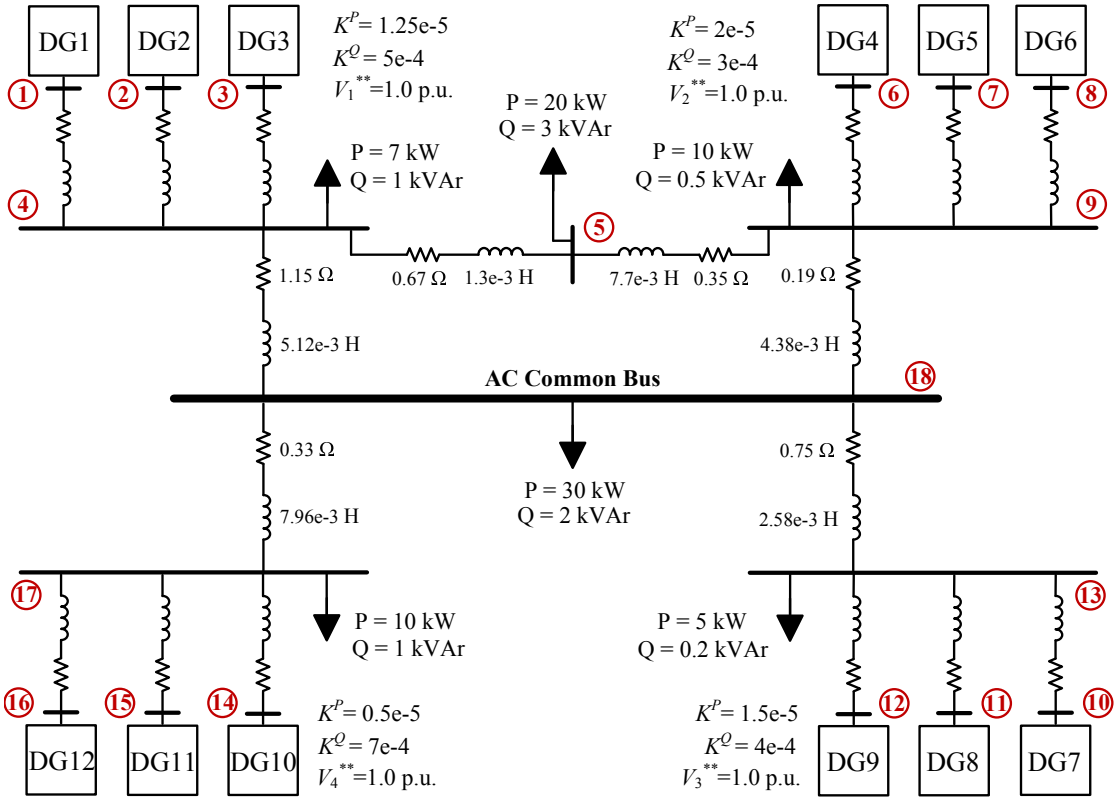

FIGURE 4.1: Single-line diagram of the case study microgrid.

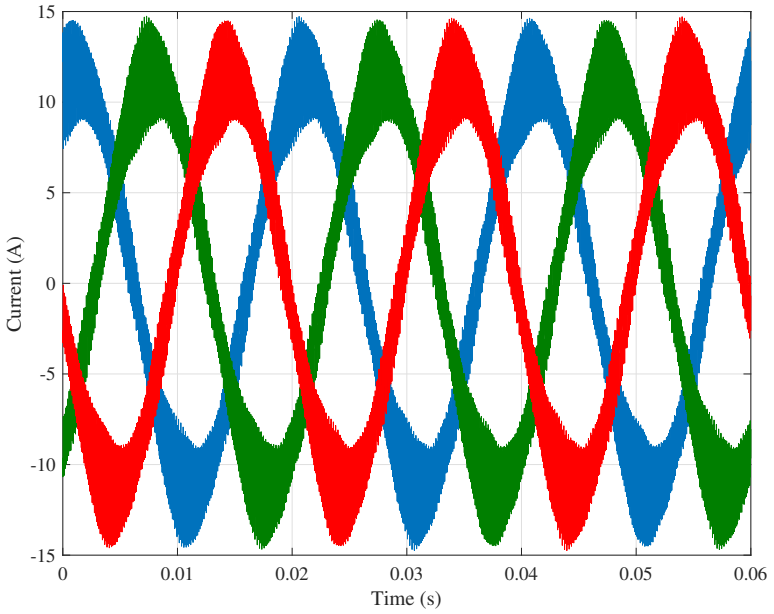

FIGURE 4.2: DG unit 1 output currents of the controlled microgrid system.

are compared against solutions obtained using the hierarchical extended power flow as initialization. Their performance in terms of convergence and CPU time is presented, and the advantages of the power flow initialization are highlighted. In this evaluation, a convergence error tolerance of 1×10^{-8} is used. On the other hand, the stability of the MG is analyzed and a comparison between the stability information in different Newton iterations is presented.

4.2.1 Case study: comparison among Newton methods using two initialization approaches

Table 4.2 shows the convergence mismatches obtained with the Newton methods using three full-cycles as initialization. In this table can be observed that the Newton methods obtain the steady-state solution with quadratic convergence rate, being the fastest the DEE method (1160.06 s) and the slowest the ND method (7365.34 s). On the other hand, the method which achieved the smallest convergence error was the END method (1.35×10^{-13}). Note that even with the fastest method, the computation of the steady-state solution is performed in the order of several minutes, which could be an inconvenient for analysis that requires the computation of the steady-state solution repeatedly.

Regarding the aforementioned, Table 4.3 shows the convergence mismatches obtained with the Newton methods using the hierarchical extended power flow solution as initialization. As shown in Table 4.3, using this initialization approach, the Newton methods

TABLE 4.2: Newton methods convergence mismatches using three full-cycles as initialization

Iter	AT	AD	ND	DEE	DF	END
1	2.53×10^{-2}	2.53×10^{-2}	2.53×10^{-2}	4.22×10^{-3}	2.53×10^{-2}	2.76×10^{-2}
2	1.23×10^{-4}	1.23×10^{-4}	1.35×10^{-4}	5.05×10^{-5}	1.29×10^{-4}	2.19×10^{-4}
3	3.24×10^{-8}	3.15×10^{-8}	4.72×10^{-7}	5.64×10^{-7}	9.02×10^{-9}	7.02×10^{-8}
4	1.92×10^{-11}	1.65×10^{-11}	4.15×10^{-9}	6.47×10^{-9}	-	1.35×10^{-13}
CPU time	4183.53 s	3823.56 s	7365.34 s	1160.06 s	5977.93 s	3935.62 s

converge in less iterations and the CPU time is reduced. Note that in the first iteration the methods achieve an error of at least 1×10^{-5}, which is an acceptable error for steady-state analysis, therefore, using only one iteration of the Newton methods the CPU time required to obtain the solution is reduced as shown in Table 4.4. Comparing the CPU times of Table 4.3 against the CPU times of Table 4.2, it is observed that the CPU times are reduced 4.88, 4.35, 4.06, 4.87, 3.35, and 4.60 times for the AT, AD, ND, DEE, DF, and END method, respectively, showing the advantage of using the hierarchical extended power flow as initialization for the Newton methods.

TABLE 4.3: Newton methods convergence mismatches using the hierarchical extended power flow solution as initialization

Iter	AT	AD	ND	DEE	DF	END
1	1.11×10^{-5}	1.11×10^{-5}	6.98×10^{-6}	8.11×10^{-5}	6.94×10^{-6}	2.54×10^{-5}
2	8.08×10^{-9}	8.10×10^{-9}	5.14×10^{-8}	1.13×10^{-6}	1.57×10^{-8}	2.42×10^{-8}
3	-	-	7.45×10^{-10}	7.99×10^{-9}	5.21×10^{-13}	1.41×10^{-13}
CPU time	1714.54 s	1758.08 s	5434.30 s	714.31 s	5348.51 s	2561.82 s

TABLE 4.4: Newton methods convergence error of one iteration using the hierarchical extended power flow solution as initialization

Iter	AT	AD	ND	DEE	DF	END
1	1.11×10^{-5}	1.11×10^{-5}	6.98×10^{-6}	8.11×10^{-5}	6.94×10^{-6}	2.54×10^{-5}
CPU time	857.27 s	879.04 s	1,811.43 s	238.10 s	1,782.83 s	853.94 s

One of the advantages of the Newton methods is that the transition matrix eigenvalues are the Floquet multipliers [28], therefore, the transition matrix of the computed solution provides information about the stability of the periodic solution [27].

In this regard, to show that the Floquet multipliers computed with the solutions shown in Table 4.4 are reliable to be used in a stability analysis, a comparison against the Floquet multipliers computed with the solutions of Table 4.3 is performed. Figure 4.3 shows the Floquet multipliers obtained using the DEE method with a convergence error of 7.99×10^{-9} and 8.11×10^{-5}. The DEE method is used to test the Floquet multipliers because its transition matrix formulation is less exact than the others [33], therefore, the largest Floquet multiplier errors are expected with the DEE method.

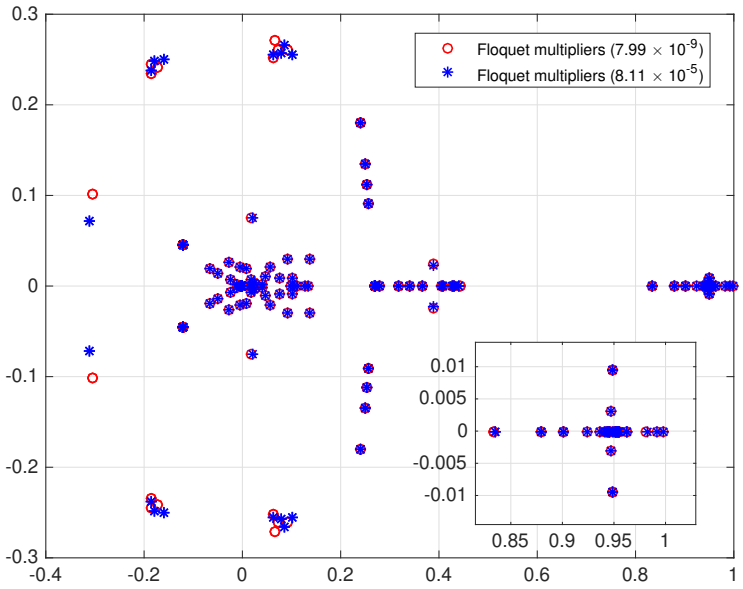

FIGURE 4.3: Floquet multipliers computed using the DEE method with different convergence error.

Note that in Figure 4.3 there are differences among the Floquet multipliers close to the center of the unitary circle, but those closest to the periphery of the unitary circle, which tell if the system is stable or unstable, are very similar. The maximum absolute Floquet multiplier is 9.9722×10^{-1} and 9.9723×10^{-1}, for the solution with an error of 7.99×10^{-9} and 8.11×10^{-5}, respectively. Therefore, it is shown that the stability information of the system is reliable for the solution with an error of 8.11×10^{-5}.

4.3 Discussions

The evaluation of the Newton Methods using two initialization approaches, i.e., three full cycles integration and the hierarchical extended power flow, was presented. The results obtained showed that using the power flow initialization, the CPU time required by the Newton methods is reduced, in the best case up to 4.88 times and in the worst

case up to 3.35 times. Furthermore, it is shown that using the power flow initialization, the first iteration of the Newton methods is reliable to obtain the stability information of the system. Regarding the aforementioned, it is shown that the Newton methods with the hierarchical extended power flow initialization are reliable and fast tools to compute the periodic steady-state solution and to analyze the stability of nonsinusoidal controlled AC microgrids.

Conclusions

The microgrid concept has emerged as an alternative to modernize the conventional electric power system. The conventional systems, which have unidirectional power flow and centralized generation, are facing serious problems due to fossil fuel depletion, environmental pollution, etc. Contrary to the conventional systems, the microgrids involve distributed generation units with renewable energy resources, energy storage systems, bidirectional power flow, and a wide controllability. These microgrid features, bring advantages such as, voltage and frequency regulation, reduction of transmission losses, ancillary services, power flow controllability, improved reliability, among others. However, while it is true that the microgrids offer special operating features, this has brought the necessity of research in different areas including, inter alia, control, protections, communication systems, component models, numerical methods and optimal design.

In this way, this thesis presented the formulation, implementation and analysis of numerical methods and component models for the steady-state computation of AC microgrids, taking into account hierarchical control schemes and the explicit commutation of power converters. Furthermore, the development and the laboratory implementation of a hierarchical control scheme for islanded AC microgrids was presented.

In the first part of the thesis, basic control schemes for AC microgrids are addressed, and stability and resonance analysis were performed. The results obtained showed that the power converters commutation process had a significant effect in the microgrid performance due to the harmonic components, resonances and interactions among DG units and controllers. Therefore, it was revealed that for microgrids the consideration of the commutation process of the power converters in the analysis was necessary in order to not overlook phenomena or undesirable behaviors in the system.

In this regard, different numerical methods for the steady-state computation of AC microgrids were addressed. A detailed description of six Newton methods was presented, additionally, their evaluation and comparison were performed. Besides, in order to reduce the computation time needed by the Newton methods, the use of advanced computing tools, such as, parallel cloud computing was included and evaluated. The analysis of

these methods showed that they are useful to compute the periodic steady-state solution of AC microgrids, but large computation time is required for large and/or stiff systems. Despite the above, it was concluded from the results obtained that the methods can compute the steady-state solutions with a high degree of detail, including harmonics, control schemes, and nonlinearities, being a reliable off-line tool for steady-state analysis.

On the other hand, the power flow method for conventional electric power systems was presented, however, since the method cannot be applied directly to AC microgrids, a new formulation for hierarchical controlled AC microgrids was formulated, which was one of the main contributions of this thesis. The proposed formulation was tested and compared against professional simulators, i.e., MATLAB/Simulink and PSCAD. Furthermore, the proposed formulation was compared against the droop-based power flow and it was shown that for both methods different results are achieved, therefore, the necessity of the new formulation was demonstrated. It was shown in the results obtained that the drawback of this method is that only the fundamental frequency can be taken into account; however, due to the power flow methods require small computation times, in the order of milliseconds, these methods can be used for practical online applications, such as, monitoring, control, optimization, etc.

An application of the extended power flow method for islanded AC microgrids was presented in the development of a hierarchical control scheme, where the optimal operating points were computed using the extended power flow. This control scheme was implemented and was online tested in a microgrid laboratory, showing a good performance for random load and generator capacity profiles. Additionally, it was shown that even with practical smart meters, which implies time delays in the communication, the control achieved the desired optimal operating objectives. Therefore, it is concluded that the application of the power flow method for the optimization of the primary control gains can be extended to practical microgrids reliably.

Finally, in order to obtain the steady-state solution of controlled AC microgrids including explicitly the commutation process of the power electronic converters without needing a prohibitive computation time, a predictor-corrector scheme was proposed. In this scheme, the hierarchical extended power flow method is used to obtain an initialization vector, which is used later in the Newton methods. The proposed scheme was evaluated using a case study microgrid and the results showed a significant reduction in the computation time required by the Newton methods. Accordingly, it was shown that this scheme is a reliable and fast tool to compute the periodic steady-state solution of controlled nonlinear AC microgrids.

Contributions

This section summarizes the main contributions from the point of view of the Author:

- The harmonic assessment of controlled AC microgrids, showing the necessity of developing models and numerical methods for detailed and reliable analysis.
- The evaluation of six Newton methods for the steady-state computation of controlled AC microgrids, showing their reliability to obtain solutions with a high degree of detail, including harmonics, control schemes, and nonlinearities.
- The application and evaluation of parallel cloud computing in three Newton methods to reduce their computation time.
- The formulation of the hierarchical extended power flow.
- The development and laboratory implementation of a hierarchical control scheme for islanded AC microgrids, using the extended power flow as an optimizer.
- The development of a predictor-corrector scheme using the Newton methods and the hierarchical extended power flow for the fast steady-state computation of controlled AC microgrids.

Future work

The methods and contributions developed in this thesis showed the following promising aspects that can be investigated in the future:

- Formulation of the hierarchical extended power flow for unbalanced systems.
- Stability and resonance evaluation of multi-microgrid systems.
- Improvement of the hierarchical control scheme by including parameter estimators.
- Development of management strategies including energy markets.
- Formulation of different control strategies for the power flow method.

Bibliography

[1] D. E. Olivares, A. Mehrizi-Sani, A. H. Etemadi, C. A. Cañizares, R. Iravani, M. Kazerani, A. H. Hajimiragha, O. Gomis-Bellmunt, M. Saeedifard, R. Palma-Behnke, G. A. Jiménez-Estévez, and N. D. Hatziargyriou. Trends in microgrid control. *IEEE Transactions on Smart Grid*, 5(4):1905–1919, July 2014. ISSN 1949-3053. doi: 10.1109/TSG.2013.2295514.

[2] R.H. Lasseter. Microgrids. In *IEEE Power Engineering Society Winter Meeting, 2002.*, volume 1, pages 305–308 vol.1, 2002.

[3] S. Chowdhury and P. Crossley. *Microgrids and Active Distribution Networks*. IET renewable energy series. Institution of Engineering and Technology, 2009. ISBN 9781849190145.

[4] C. Li, S. K. Chaudhary, J. C. Vasquez, and J. M. Guerrero. Power flow analysis algorithm for islanded lv microgrids including distributed generator units with droop control and virtual impedance loop. In *2014 IEEE Applied Power Electronics Conference and Exposition - APEC 2014*, pages 3181–3185, March 2014. doi: 10.1109/APEC.2014.6803760.

[5] J. Schiffer, D. Zonetti, R. Ortega, A. Stankovic, T. Sezi, and J. Raisch. A survey on modeling of microgrids - from fundamental physics to phasors and voltage sources. *ArXiv*, May 2015.

[6] K. Balamurugan and D. Srinivasan. Review of power flow studies on distribution network with distributed generation. In *Power Electronics and Drive Systems (PEDS), 2011 IEEE Ninth International Conference on*, pages 411–417, Dec 2011. doi: 10.1109/PEDS.2011.6147281.

[7] Xiaoqiang Guo, Zhigang Lu, Baocheng Wang, Xiaofeng Sun, Lei Wang, and J.M. Guerrero. Dynamic phasors-based modeling and stability analysis of droop-controlled inverters for microgrid applications. *Smart Grid, IEEE Transactions on*, 5(6):2980–2987, Nov 2014. ISSN 1949-3053. doi: 10.1109/TSG.2014.2331280.

[8] M. Rana, Wei Xiang, and Erric Wang. Smart grid state estimation and stabilisation. *International Journal of Electrical Power and Energy Systems*, 102:152 – 159, 2018. ISSN 0142-0615. doi: https://doi.org/10.1016/j.ijepes.2018.03.007.

[9] N. Hatziargyriou, H. Asano, R. Iravani, and C. Marnay. Microgrids. *Power and Energy Magazine, IEEE*, 5(4):78–94, July 2007. ISSN 1540-7977. doi: 10.1109/MPAE.2007.376583.

[10] J. Rocabert, A. Luna, F. Blaabjerg, and P. Rodríguez. Control of power converters in ac microgrids. *IEEE Transactions on Power Electronics*, 27(11):4734–4749, Nov 2012. ISSN 0885-8993. doi: 10.1109/TPEL.2012.2199334.

[11] J. M. Guerrero, J. C. Vasquez, J. Matas, L. G. de Vicuna, and M. Castilla. Hierarchical control of droop-controlled ac and dc microgrids: A general approach toward standardization. *IEEE Transactions on Industrial Electronics*, 58(1):158–172, Jan 2011. ISSN 0278-0046.

[12] R. C. Schaefer. Art of generator synchronizing. *IEEE Transactions on Industry Applications*, 53(1):751–757, Jan 2017. ISSN 0093-9994. doi: 10.1109/TIA.2016.2602215.

[13] F.M. Gardner. *Phaselock Techniques*. Wiley, 2005. ISBN 9780471732686.

[14] Saeed Golestan, Josep M Guerrero, and Juan C Vasquez. Three-phase plls: A review of recent advances. *IEEE Transactions on Power Electronics*, 32(3):1894–1907, 2017.

[15] J. A. P. Lopes, C. L. Moreira, and A. G. Madureira. Defining control strategies for microgrids islanded operation. *IEEE Transactions on Power Systems*, 21(2):916–924, May 2006. ISSN 0885-8950. doi: 10.1109/TPWRS.2006.873018.

[16] J.M. Guerrero, L. Garcia De Vicuna, J. Matas, M. Castilla, and J. Miret. A wireless controller to enhance dynamic performance of parallel inverters in distributed generation systems. *IEEE Transactions on Power Electronics*, 19(5):1205–1213, Sept 2004. ISSN 0885-8993. doi: 10.1109/TPEL.2004.833451.

[17] Q.C. Zhong and T. Hornik. *Control of Power Inverters in Renewable Energy and Smart Grid Integration*. Wiley - IEEE. Wiley, 2012. ISBN 9781118481790.

[18] Frede Blaabjerg, Remus Teodorescu, Marco Liserre, and Adrian V Timbus. Overview of control and grid synchronization for distributed power generation systems. *IEEE Transactions on industrial electronics*, 53(5):1398–1409, 2006.

[19] Q. Shafiee, J. M. Guerrero, and J. C. Vasquez. Distributed secondary control for islanded microgrids: A novel approach. *IEEE Transactions on Power Electronics*, 29(2):1018–1031, Feb 2014. ISSN 0885-8993. doi: 10.1109/TPEL.2013.2259506.

[20] Xisheng Tang, Wei Deng, and Zhiping Qi. Investigation of the dynamic stability of microgrid. *Power Systems, IEEE Transactions on*, 29(2):698–706, March 2014. ISSN 0885-8950. doi: 10.1109/TPWRS.2013.2285585.

[21] Mohammad M. Hashempour, Mehdi Savaghebi, Juan C. Vasquez, and Josep M. Guerrero. Hierarchical control for voltage harmonics compensation in multi-area microgrids. In *Diagnostics for Electrical Machines, Power Electronics and Drives (SDEMPED), 2015 IEEE 10th International Symposium on*, pages 415–420, Sept 2015. doi: 10.1109/DEMPED.2015.7303723.

[22] I. Lorzadeh, H.A. Abyaneh, M. Savaghebi, and J.M. Guerrero. A hierarchical control scheme for reactive power and harmonic current sharing in islanded microgrids. In *Power Electronics and Applications (EPE'15 ECCE-Europe), 2015 17th European Conference on*, pages 1–10, 2015.

[23] S.S. Acevedo and M. Molinas. Power electronics modeling fidelity: Impact on stability estimate of micro-grid systems. In *Innovative Smart Grid Technologies Asia (ISGT), 2011 IEEE PES*, pages 1–8, Nov 2011.

[24] Xiongfei Wang, F. Blaabjerg, and Weimin Wu. Modeling and analysis of harmonic stability in an ac power-electronics-based power system. *Power Electronics, IEEE Transactions on*, 29(12):6421–6432, Dec 2014. ISSN 0885-8993. doi: 10.1109/TPEL.2014.2306432.

[25] F. Katiraei and M.R. Iravani. Power management strategies for a microgrid with multiple distributed generation units. *IEEE Transactions on Power Systems*, 21 (4):1821–1831, Nov 2006. ISSN 0885-8950.

[26] P. Moreno and A. Ramirez. Implementation of the numerical laplace transform: A review task force on frequency domain methods for emt studies, working group on modeling and analysis of system transients using digital simulation, general systems subcommittee, ieee power engineering society. *IEEE Transactions on Power Delivery*, 23(4):2599–2609, Oct 2008. ISSN 0885-8977. doi: 10.1109/TPWRD.2008.923404.

[27] T.S. Parker and L. Chua. *Practical Numerical Algorithms for Chaotic Systems*. Springer New York, 2012. ISBN 9781461234869.

[28] A.H. Nayfeh and B. Balachandran. *Applied Nonlinear Dynamics: Analytical, Computational and Experimental Methods*. Wiley Series in Nonlinear Science. Wiley, 2008. ISBN 9783527617555.

[29] A Medina, J. Segundo, P. Ribeiro, W. Xu, K.L. Lian, G.W. Chang, V. Dinavahi, and N.R. Watson. Harmonic analysis in frequency and time domain. *IEEE Transactions on Power Delivery*, 28(3):1813–1821, July 2013. ISSN 0885-8977.

[30] Jr. Aprille, T.J. and Timothy N. Trick. Steady-state analysis of nonlinear circuits with periodic inputs. *Proceedings of the IEEE*, 60(1):108–114, Jan 1972. ISSN 0018-9219.

[31] A. Semlyen and A. Medina. Computation of the periodic steady state in systems with nonlinear components using a hybrid time and frequency domain methodology. *IEEE Transactions on Power Systems*, 10(3):1498–1504, Aug 1995. ISSN 0885-8950. doi: 10.1109/59.466497.

[32] Juan Segundo-Ramírez and A Medina. An enhanced process for the fast periodic steady state solution of nonlinear systems by Poincaré map and extrapolation to the limit cycle. *International Journal of Nonlinear Sciences and Numerical Simulation*, 11(8):661–670, Aug 2010.

[33] Juan Segundo-Ramírez and A Medina. computation of the steady state solution of nonlinear power systems by extrapolation to the limit cycle using a discrete exponential expansion method. *International Journal of Nonlinear Sciences and Numerical Simulation*, 11(8):655–660, Aug 2010.

[34] IEEE recommended practice for industrial and commercial power system analysis. *IEEE Std 399-1990*, pages 1–384, Dec 1990.

[35] J. Segundo-Ramirez and A Medina. Modeling of FACTS devices based on SPWM VSCs. *IEEE Transactions on Power Delivery*, 24(4):1815–1823, Oct 2009. ISSN 0885-8977.

[36] M. Armbrust, A. Fox, R. Griffith, A. D. Joseph, R H. Katz, A. Konwinski, G. Lee, D. A. Patterson, A Rabkin, I. Stoica, and M. Zaharia. Above the clouds: A berkeley view of cloud computing. *Tech. Rep. UCB/EECS-2009-28, EECS Department, U.C. Berkeley*, pages 1–23, February 2009.

[37] W. Stevenson and J. Grainger. *Power System Analysis*. McGraw-Hill series in electrical and computer engineering: Power and energy. McGraw-Hill Education (India) Pvt Limited, 2003.

[38] H. Saadat. *Power System Analysis*. McGraw-Hill series in electrical and computer engineering. McGraw-Hill, 2002.

[39] M. M. A. Abdelaziz, H. E. Farag, E. F. El-Saadany, and Y. A. R. I. Mohamed. A novel and generalized three-phase power flow algorithm for islanded microgrids using a newton trust region method. *IEEE Transactions on Power Systems*, 28(1): 190–201, Feb 2013. ISSN 0885-8950. doi: 10.1109/TPWRS.2012.2195785.

[40] C. Li, S. K. Chaudhary, M. Savaghebi, J. C. Vasquez, and J. M. Guerrero. Power flow analysis for low-voltage ac and dc microgrids considering droop control and virtual impedance. *IEEE Transactions on Smart Grid*, 2016. ISSN 1949-3053. doi: 10.1109/TSG.2016.2537402.

[41] Islam Ziouani, Djamel Boukhetala, Abdel-Moumen Darcherif, Bilal Amghar, and Ikram El Abbassi. Hierarchical control for flexible microgrid based on three-phase voltage source inverters operated in parallel. *International Journal of Electrical Power and Energy Systems*, 95:188 – 201, 2018. ISSN 0142-0615. doi: https://doi.org/10.1016/j.ijepes.2017.08.027.

[42] Adam Hirsch, Yael Parag, and Josep Guerrero. Microgrids: A review of technologies, key drivers, and outstanding issues. *Renewable and Sustainable Energy Reviews*, 90:402 – 411, 2018. ISSN 1364-0321.

[43] A. Bidram and A. Davoudi. Hierarchical structure of microgrids control system. *IEEE Transactions on Smart Grid*, 3(4):1963–1976, Dec 2012. ISSN 1949-3053. doi: 10.1109/TSG.2012.2197425.

[44] J. W. Simpson-Porco, Q. Shafiee, F. Dörfler, J. C. Vasquez, J. M. Guerrero, and F. Bullo. Secondary frequency and voltage control of islanded microgrids via distributed averaging. *IEEE Transactions on Industrial Electronics*, 62(11):7025–7038, Nov 2015. ISSN 0278-0046. doi: 10.1109/TIE.2015.2436879.

[45] W. F. Tinney and C. E. Hart. Power flow solution by newton's method. *IEEE Transactions on Power Apparatus and Systems*, PAS-86(11):1449–1460, Nov 1967. ISSN 0018-9510. doi: 10.1109/TPAS.1967.291823.

[46] L. Ren and P. Zhang. Generalized microgrid power flow. *IEEE Transactions on Smart Grid*, PP(99):1–1, 2018. ISSN 1949-3053. doi: 10.1109/TSG.2018.2813080.

[47] N. L. Díaz, E. A. Coelho, J. C. Vasquez, and J. M. Guerrero. Stability analysis for isolated ac microgrids based on pv-active generators. In *2015 IEEE Energy Conversion Congress and Exposition (ECCE)*, pages 4214–4221, Sept 2015. doi: 10.1109/ECCE.2015.7310255.

[48] Ahmet Mete Vural. Interior point-based slack-bus free-power flow solution for balanced islanded microgrids. *International Transactions on Electrical Energy Systems*, 26(5):968–992, 2016. ISSN 2050-7038. doi: 10.1002/etep.2117.

[49] A. Bidram, F. L. Lewis, and A. Davoudi. Distributed control systems for small-scale power networks: Using multiagent cooperative control theory. *IEEE Control Systems*, 34(6):56–77, Dec 2014. ISSN 1066-033X. doi: 10.1109/MCS.2014.2350571.

[50] Francesco Marra and Guangya Yang. Chapter 10 - decentralized energy storage in residential feeders with photovoltaics. In Pengwei DuNing Lu, editor, *Energy Storage for Smart Grids*, pages 277 – 294. Academic Press, Boston, 2015. ISBN 978-0-12-410491-4.

[51] T. L. Vandoorn, J. C. Vasquez, J. De Kooning, J. M. Guerrero, and L. Vandevelde. Microgrids: Hierarchical control and an overview of the control and reserve management strategies. *IEEE Industrial Electronics Magazine*, 7(4):42–55, Dec 2013. ISSN 1932-4529. doi: 10.1109/MIE.2013.2279306.

[52] R. A. Mohr, R. Moreno, and H. Rudnick. Insertion of distributed generation into rural feeders. In *2009 CIGRE/IEEE PES Joint Symposium Integration of Wide-Scale Renewable Resources Into the Power Delivery System*, pages 1–10, July 2009.

[53] Robert Lasseter, Abbas Akhil, Chris Marnay, John Stevens, Jeff Dagle, Ross Guttromson, Sakis A. Meliopoulous, Robert Yinger, and Joe Eto. The CERTS MicroGrid Concept - White Paper on Integration of Distributed Energy Resources. Technical report, U.S. Department of Energy, April 2002.

[54] L. Zhang, H. Xin, Z. Wang, and D. Gan. A decentralized quasi-hierarchical control scheme for droop-controlled ac island microgrids. In *2016 IEEE Power and Energy Society General Meeting (PESGM)*, pages 1–5, July 2016. doi: 10.1109/PESGM.2016.7741600.

[55] L. Che, M. Shahidehpour, A. Alabdulwahab, and Y. Al-Turki. Hierarchical coordination of a community microgrid with ac and dc microgrids. *IEEE Transactions on Smart Grid*, 6(6):3042–3051, Nov 2015. ISSN 1949-3053. doi: 10.1109/TSG.2015.2398853.

[56] Eleonora Riva Sanseverino, Ninh Nguyen Quang, Maria Luisa Di Silvestre, Josep M. Guerrero, and Chendan Li. Optimal power flow in three-phase islanded microgrids with inverter interfaced units. *Electric Power Systems Research*, 123(Supplement C):48 – 56, 2015. ISSN 0378-7796. doi: https://doi.org/10.1016/j.epsr.2015.01.020.

[57] E. R. Sanseverino, N. Q. Nguyen, M. L. Di Silvestre, G. Zizzo, F. de Bosio, and Q. T. T. Tran. Frequency constrained optimal power flow based on glow-worm

swarm optimization in islanded microgrids. In *2015 AEIT International Annual Conference (AEIT)*, pages 1–6, Oct 2015. doi: 10.1109/AEIT.2015.7415233.

[58] C. Deckmyn, T. Vandoorn, J. Van de Vyver, J. Desmet, and L. Vandevelde. A microgrid multilayer control concept for optimal power scheduling and voltage control. *IEEE Transactions on Smart Grid*, 2017. ISSN 1949-3053. doi: 10.1109/TSG.2017.2658865.

[59] R. A. Mohr, R. Moreno, and H. Rudnick. Insertion of distributed generation into rural feeders. In *2009 CIGRE/IEEE PES Joint Symposium Integration of Wide-Scale Renewable Resources Into the Power Delivery System*, pages 1–10, July 2009.

[60] j. zhou, S. Kim, H. Zhang, Q. Sun, and R. Han. Consensus-based distributed control for accurate reactive, harmonic and imbalance power sharing in microgrids. *IEEE Transactions on Smart Grid*, PP(99):1–1, 2016. ISSN 1949-3053. doi: 10.1109/TSG.2016.2613143.

[61] Y. Zhu, F. Zhuo, F. Wang, B. Liu, and Y. Zhao. A wireless load sharing strategy for islanded microgrid based on feeder current sensing. *IEEE Transactions on Power Electronics*, 30(12):6706–6719, Dec 2015. ISSN 0885-8993. doi: 10.1109/TPEL.2014.2386851.

[62] H. Zhang, S. Kim, Q. Sun, and J. u. Distributed adaptive virtual impedance control for accurate reactive power sharing based on consensus control in microgrids. *IEEE Transactions on Smart Grid*, PP(99):1–13, 2016. ISSN 1949-3053. doi: 10.1109/TSG.2015.2506760.

[63] F. H. Dupont, J. Zaragoza, C. Rech, and J. R. Pinheiro. A new method to improve the total efficiency of parallel converters. In *2013 Brazilian Power Electronics Conference*, pages 210–215, Oct 2013. doi: 10.1109/COBEP.2013.6785117.

[64] A. C. Luna, N. L. Diaz, M. Graells, J. C. Vasquez, and J. M. Guerrero. Mixed-integer-linear-programming-based energy management system for hybrid pv-wind-battery microgrids: Modeling, design, and experimental verification. *IEEE Transactions on Power Electronics*, 32(4):2769–2783, April 2017. ISSN 0885-8993. doi: 10.1109/TPEL.2016.2581021.

[65] M. Han, D. Xu, and L. Wan. Hierarchical optimal power flow control for loss minimization in hybrid multi-terminal hvdc transmission system. *CSEE Journal of Power and Energy Systems*, 2(1):40–46, March 2016. doi: 10.17775/CSEEJPES.2016.00007.

[66] K. R. C. Mamandur and R. D. Chenoweth. Optimal control of reactive power flow for improvements in voltage profiles and for real power loss minimization. *IEEE*

Transactions on Power Apparatus and Systems, PAS-100(7):3185–3194, July 1981. ISSN 0018-9510. doi: 10.1109/TPAS.1981.316646.

[67] L. Meng, A. Luna, E. R. Díaz, B. Sun, T. Dragicevic, M. Savaghebi, J. C. Vasquez, J. M. Guerrero, M. Graells, and F. Andrade. Flexible system integration and advanced hierarchical control architectures in the microgrid research laboratory of aalborg university. *IEEE Transactions on Industry Applications*, 52(2):1736–1749, March 2016. ISSN 0093-9994. doi: 10.1109/TIA.2015.2504472.

[68] E. J. Palacios-García, Y. Guan, M. Savaghebi, J. C. Vásquez, J. M. Guerrero, A. Moreno-Munoz, and B. S. Ipsen. Smart metering system for microgrids. In *IECON 2015 - 41st Annual Conference of the IEEE Industrial Electronics Society*, pages 003289–003294, Nov 2015. doi: 10.1109/IECON.2015.7392607.

[69] Chance Elliott, Vipin Vijayakumar, Wesley Zink, and Richard Hansen. National instruments labview: A programming environment for laboratory automation and measurement. *JALA: Journal of the Association for Laboratory Automation*, 12(1): 17–24, 2007. doi: 10.1016/j.jala.2006.07.012.